Materials & Design 269 (2026) 116785

Contents lists available at ScienceDirect

Materials & Design

journal homepage: www.elsevier.com/locate/matdes

Microstructure and creep behavior of antimony containing high silver solder alloy Sn-3.9Ag-0.6Cu-3.0Sb

Christian Kreiner [a,*], Michael Konrad Eusterholz [b,c], Gabriel Benedet Dutra [d], Daniel Zeitler [a], Heinz Werner Höppel [e], Ulrich Tetzlaff [a,*]

[a] Technische Hochschule Ingolstadt, Esplanade 10, Ingolstadt 85049, Germany
[b] Institute for Applied Materials – Material Science, Karlsruhe Institute of Technology, Engelbert-Arnold-Straße 4, Karlsruhe 76131, Germany
[c] Karlsruhe Nano Micro Facility (KNMFi), Karlsruhe Institute of Technology, Hermann-von-Helmholtz-Platz 1, Eggenstein-Leopoldshafen 76344, Germany
[d] Department of Mobility Engineering, Federal University of Santa Catarina, Joinville, Brazil
[e] Institute of General Materials Properties MSEI, Friedrich-Alexander-University Erlangen-Nuremberg, 91058, Germany

ARTICLE INFO

Keywords:
Compression creep
SAC 396+
Solder alloys
SbSn precipitates
X-ray diffraction (XRD)

ABSTRACT

Antimony containing Sn-3.9Ag-0.6Cu-3.0Sb (SAC 396 +) is a high reliability solder alloy but its microstructure and creep behavior is not sufficiently investigated yet. In this paper the correlation between microstructure, using SEM, TEM, and XRD, and compression creep properties was investigated. Furthermore, a comparison in creep performance between SAC 396 + and Sn-3.8Ag-0.7Cu (SAC 387) was drawn, and the long-term microstructure evolution until 1500 h at 125 °C was compared. For SAC 396+, microstructure investigations of pre-aged (24 h at 125 °C) bulk samples revealed that Sb is mainly dissolved in β-Sn (Sb_2Sn_{23}, tetragonal, I41/amd), whereas some fine SbSn precipitates ($Sb_{0.49}Sn_{0.51}$, rhombohedral, R-3 m) were found in β-Sn. Compression creep tests were performed at temperatures between 35 °C and 125 °C and at stresses between 7.5 MPa and 32.5 MPa. Stress exponents were in the range of 7.4 to 7.5 at 100 °C or below, and 4.8 at 125 °C. Activation energies were in the range between 84.7 kJ/mol and 99.6 kJ/mol, indicating dislocation creep, controlled by pipe diffusion or by lattice diffusion. Overall, Sb hardened SAC 396 + showed better creep performance at all tested temperatures, as well as after isothermal ageing at 125 °C for 24 h, 500 h, or 1500 h.

1. Introduction

Lead containing solder alloys have been widely used for several years in car-electronic products. Due to restrictions in the European Union, the usage of lead in electronic products has been restricted since 2006. Therefore, ternary tin-based Sn-Ag-Cu (SAC) alloys have been adopted to replace lead containing alloys. Solder alloy Sn-3.9Ag-0.6Cu-3.0Sb (SAC396 +) is used in the automotive industry in electronic packages, due to enhanced thermal fatigue resistance and high reliability in harsh environments [1–4]. Since the solubility of both Ag and Cu in Sn is very low, the microstructure of these Sn-Ag-Cu consists of dendrites of β-Sn and binary or tertiary eutectic regions, composed of β-Sn and Ag_3Sn and/or Cu_6Sn_5 intermetallic precipitates. Especially Ag_3Sn hinders the dislocation movement and increases creep strength [5,6] through Orowan strengthening and dislocation detachment from Ag_3Sn intermetallic particles, whereby this effect is more pronounced, when the Ag-content in Sn-Ag-Cu is increased [7–10]. On the other hand, eutectic Cu_6Sn_5 seems to have only a slight effect on increasing the creep resistance in comparison to Ag_3Sn, which is due to their lower volume fraction and therefore larger interparticle spacing [11]. In autonomous vehicles, a high level of reliability of the assistance systems is safety-relevant, which includes a high reliability of the involved electronic devices and consequently of the included solder joints [12,13]. Since temperatures in service condition could reach 150 °C (423,15 K), which is about 0.85 homologous temperature, or in future applications even 200 °C (473,15 K), which correspond to about 0.95 homologous temperature, a high creep resistant Sn-Ag-Cu solder alloy is fundamental to achieve the required high reliability of electronic packages. Beyond that, solder-joints in service also experience thermomechanical stresses due to high differences in the coefficient of thermal expansion of the different materials around the actual solder joint. The typical temperature changes in service therefore lead to high stresses and these, in combination with high homologous temperatures, lead to ageing of the solder joints. Today, a variety of Sn-Ag-Cu alloys have been developed. Since

* Corresponding authors.
E-mail addresses: extern.christian.kreiner@thi.de (C. Kreiner), Ulrich.tetzlaff@thi.de (U. Tetzlaff).

https://doi.org/10.1016/j.matdes.2026.116785
Received 3 April 2026; Received in revised form 4 August 2026; Accepted 12 August 2026
Available online 12 August 2026

pure ternary Sn-Ag-Cu solder joints could not ensure such high reliability, due to coarsening of intermetallic particles, and due to growth of intermetallic layers at the solder-substrate boundaries, further elements like antimony (Sb), indium (In), nickel (Ni), and/or bismuth (Bi), or vanadium are added for improving the microstructure and mechanical properties, stabilizing and refining the microstructure [2,4,14–18]. Adding Bi to Sn-Ag-Cu improve the yield strength and ultimate tensile strength [19], and lower the melting temperature if 2 wt-% or more Bi is added [20]. However, Bi addition lower the ductility [21] and lead to brittleness of the solder joint, which is problematic for drop shock resistance in mobile electronic devices. Sb additions may improve the ductility of solder joints [22] and lead to solid solution hardening of β-Sn, but with only a slight improvement in creep resistance, due to the small atomic size mismatch between Sb and Sn of around 3.2 %, whereas higher Sb concentrations of 1.5 wt-% or higher could lead to fine SbSn-precipitates, which significantly improve the creep resistance in comparison to solid solution hardening of dissolved Sb [23–26]. Furthermore, it was found that 3.0 wt-% Sb is an optimal concentration, regarding an increase in ultimate tensile strength, due to solid solution hardening and SbSn particle hardening [27]. SbSn precipitates crystallizes in a rhombohedral R-3 m structure, with a slight deviation in the angle α of 89.8°, which is close to the initially assumed 90° of the NaCl-type Fm-3 m cubic structure, and it was found, that SbSn shares an interface with both β-Sn (I41/amd, tetragonal crystal structure) and Cu_6Sn_5-particles ($P6_3/mmc$, hexagonal crystal structure) [28]. In this paper, we investigate the creep properties of SAC 396 + and compare it to Sn-3.8Ag-0.7Cu (SAC 387), which is an alloy with comparable Ag and Cu content, but without Sb addition, to evaluate the effect of Sb on the microstructure evolution and creep strengthening of SAC 396 + .

2. Materials and methods

2.1. Sample preparation

Pre-alloyed material of Sb containing SAC alloy Sn-3.9Ag-0.6Cu-3.0Sb (SAC 396 +) and of a near-eutectic, basic SAC alloy Sn-3.8Ag-0.7Cu (SAC 387) were supplied in form of bars by *Stannol GmbH & Co. KG, Velbert, Germany*. The composition was confirmed through X-ray fluorescence analysis. The material was cast in a heated aluminum mold, in which the round casting channel of the mold was oriented 60° to the horizontal plane to ensure as few grains as possible with a preferred crystallographic orientation of <110> . Thereby, cooling takes place with slow cooling rates between 0.5 °C/s and 1.0 °C/s. After the cooling process was finished, the cast rod was stored at −10 °C to slow down diffusion and therefore to prevent the microstructure from uncontrolled coarsening at room temperature. For further processing, the cast rod was cut into cylindrical samples using a precision cutting machine *Accutom-5* by *Struers*. The cylindrical samples were pre-aged for 24 h at 125 °C to reduce internal stress and to allow storage at room temperature by reducing the driving force for further microstructure coarsening [29,30]. Two cast rods were selected and annealed at 125 °C for 500 h and 1500 h, respectively, and four creep samples were prepared from each cast rod to investigate the long-term microstructure evolution and the influence of a longer ageing time on the creep properties. For the actual creep test, both front surfaces of each sample were grinded with 4000 SiC-paper to ensure as little friction as possible between the sample surface and a polished ceramic stamp, respectively. The final dimensions of the compression creep samples were 5.00 ± 0.05 mm in diameter and 7.50 ± 0.05 mm in height, resulting in an aspect ratio of 1.5. For examining the microstructure after the finished creep experiments, cross sections and longitudinal sections of creep samples, which were creep tested at 35 °C, 50 °C, and 100 °C, each with an initial stress of 20 MPa, are mounted in *EpoFix* slow-curing transparent acrylic resin by *Struers*, grinded with SiC-paper, polished with colloidal silica and finally vibratory polished for 3 min, using *Vibropol* and *Eposil-M* by *ATM*.

2.2. Characterization of the microstructure

2.2.1. SEM, EDS and EBSD analysis

For microstructure characterization, a CLARA field emitter scanning electron microscope (SEM) by *Tescan Group, Brno, Czech Republic* was used in combination with a *Xflash 6130* energy dispersive spectroscopy (EDS) detector from *Bruker Corp., Billerica, USA*. Since the I41/amd crystal cell of β-Sn shows anisotropic properties [31], electron back scatter detection (EBSD) maps of the cross sections of discrete samples were taken, using an *e-flash* EBSD detector from *Bruker Corp., Billerica, USA*. The surface was scanned at an angle of 70° to the horizontal plane. The EBSD maps and EDS spectra were in each case analyzed, using the Bruker Software *Esprit 2.3*. Before each SEM examination, a plasma cleaner inside the SEM was used to remove the oxide layer on the sample surface.

2.2.2. Phase diagram simulation by CALPHAD method

Equilibrium solidification and room-temperature stable phases were simulated using *Thermo-Calc TC 2023b* together with the TSC Solder Alloy Solutions database *TCSLD4 Solder Alloys v4.2* by *Thermo-Calc Software AB, Solna, Sweden*.

2.2.3. X-ray diffraction (XRD) analysis

For evaluating all existing phases in the alloy, X-ray diffraction patterns of both alloys SAC 396+ and SAC 387 were recorded, by means of an *EMPYREAN SERIE 2 X*-ray diffractometer from *PANalytical B.V., Almelo, Netherlands*, whereby the X-rays were generated by Cobalt with a discrete K-α wavelength of λ = 1.78901 Å. Thereby, a Bragg Brentano setting was used to analyze the alloys in powder form, which were prepared from the 24 h at 125 °C pre-aged samples, using a diamond file. For analyzing the XRD-spectra, the software *High Score* from *PANalytical* with a database *ICSD FIZ Karlsruhe 2016–1* was used.

2.2.4. Transmission electron microscopy (TEM) analysis

TEM lamellae were prepared by FIB milling using a *Strata 400 S* dual-beam facility from *FEI Company, Hillsboro, United States*. TEM investigations were conducted in a *Themis 300 probe corrected (S)TEM* from *Thermo Fisher Scientific, Waltham, USA,* at 300 kV and equipped with a *Super-X* EDX detector. SAED patterns were indexed by using *CrystBox 1.1* [32].

2.3. Compression creep measurements

Compression creep tests were performed on bulk samples of SAC 396 + and SAC 387 at 35 °C, 50 °C, 85 °C, 100 °C, and 125 °C and under initial stresses ranging from 7.5 MPa to 32.5 MPa in order to determine stress exponents and activation energies. Before creep testing, the height and diameter of each sample were measured using a micrometer. Thermo-Calc was used for calculating the thermal expansivity (CTE) of β-Sn in SAC 396+, which is shown in Table 1.

The compression creep tests were carried out with a constant load setting. The specimen was heated in a chamber oven and after the target temperature was reached, the temperature was maintained constant for one hour before the experiment was started. During the experiment, one thermocouple was in contact with the gauge length of the specimen, whereby the temperature was stable to within ± 1 °C. The applied force

Table 1
Calculated CTE values, using Thermo-Calc simulation.

Temperature	CTE in 1/°C (Thermo-Calc)
35 °C	2.23E-05
50 °C	2.27E-05
85 °C	2.36E-05
100 °C	2.40E-05
125 °C	2.46E-05

was measured using a 2 kN load cell and the strain of the sample was recorded with an extensometer. During creep testing, from time to time, the true strain rate was calculated and plotted in logarithmic form against the true strain, to check if a quasi-stable state was reached. According to *Kanjilal et al.* [33] in a compression creep test of a Sn-Ag-Cu alloy, a quasi-stable state is considered to be reached when the slope of the log strain rate versus strain curve exhibits a plateau with a defined gradient between 5 and 7, which corresponds to the expected stress exponent of a basic SAC alloy and is therefore used as an approximation. If the slope of the curve remained constant within this plateau for at least 0.5 % creep strain, the quasi-steady state was considered to have been reached, and the creep test was stopped. The slope of the true strain versus time curve within the previously defined quasi steady state region then corresponds to the secondary creep strain rate. The corresponding true stress value was calculated by averaging the calculated true stress values in this quasi steady state region.

3. Results and discussion

3.1. Microstructure of the initial state

3.1.1. Phase diagram simulation by CALPHAD method

In Fig. 1-*a*, an isopleth diagram of SAC 396 + with a varying Sb content between 0 and 5 wt-%, shows a sequence of stable phases in equilibrium condition during solidification, whereby in Fig. 1-*b*, the volume fraction of each stable phase between room temperature and melting temperature is shown. The matrix phase β-Sn grows in a non-faceted dendrite growth [34] and the volume fraction of primary β-Sn increases with further undercooling [35]. Since there is no significant solubility of Ag and Cu in β-Sn at room temperature (25 °C), the intermetallic Ag_3Sn- and Cu_6Sn_5-particles are formed in a eutectic reaction during the solidification process. *Snugovsky et al.* [36] examined the solubility of Ag and Cu in Sn, by using a SAC 387 alloy, and confirmed the solid solubility values of 0.04 wt-% Ag and 0.006 wt-% Cu. Using the eutectic concentrations of 3.5 wt-% Ag and 0.9 wt-% Cu, the calculated distribution coefficients were k = 0.011 for Ag and k = 0.007 for Cu [36]. Considering the sequences of phases solidifying during solidification, the first solid phase is the orthorhombic (Pmmn) Ag_3Sn phase, which is formed in liquid. Thereafter, the tetragonal β-Sn phase with a I41/amd crystal structure, and finally the hexagonal (P63/mmc) high temperature η-Cu_6Sn_5 phase is formed in liquid. This copper phase transforms into the monoclinic (C12/c1) η'-Cu_6Sn_5 phase below 186.5 °C by a solid-state reaction. As Thermo-Calc software suggests, an antimony containing cubic (Fm-3 m) SbSn-phase precipitates below 174.6 °C by consuming Sb, which before that, is dissolved in the β-Sn matrix (Fig. 1-*b*).

When comparing the volume fraction of equilibrium particle phases at 25 °C, SbSn has the highest volume fraction with 7 vol-%, Ag_3Sn has the second highest with 4 vol-%, and η'-Cu_6Sn_5 has the smallest volume fraction with 1 vol-%. Furthermore, SbSn has a composition of 51 wt-% Sn and 49 wt-% Sb, which is in accordance with the $Sb_{0.49}Sn_{0.51}$ phase found by *Norén et al.* [37]. Moreover, the weight percentage of Sb in the β-Sn-matrix is relatively small with 0.8 wt-% at 25 °C. These results are in agreement with the literature: CALPHAD investigations by *Zaimi et al.* [2] of Sn-3.0Ag-0.5Cu-xSb (x = 0.5 wt-% or 1.5 wt-% Sb) revealed a transformation of η-Cu_6Sn_5 to η'-Cu_6Sn_5, but at a slightly lower temperature of around 183 °C, and also showed the formation of SbSn precipitates during a solid-state reaction after 0.5 wt-% Sb, as well as after 1.5 wt-% Sb were added [2]. *Tan et al.* [22] declared for a Sn-37Bi-xSb alloy by using synchrotron powder X-Ray diffraction that cubic SbSn precipitates (Pm-3 m) could only be detected after adding 3 wt-% Sb to the alloy. Furthermore, *Chantaramanee et al.* [38] investigated the microstructure Sn-0.7Ag-0.5Cu-*x*Bi-*x*Sb solder alloy with addition of *x* = 0, 1, 2, and 3 wt-%, where after adding 3 wt-% Sb, SbSn precipitates were detected by using x-ray diffraction analysis (XRD) [38].

3.1.2. SEM and EDS measurements

As can be seen in Fig. 2-*a*, after casting SAC 396+ with a cooling rate between 0.5 °C/s and 1.0 °C/s and pre-ageing for 24 h at 125 °C, the microstructure consists of β-Sn dendrites, which are fully surrounded by eutectic regions (56.8 vol-%), containing intermetallic Ag_3Sn and/or Cu_6Sn_5 particles. These Cu_6Sn_5 particles appear darker, due to the element Cu being the lightest of the present alloying elements with 63.55 g/mol [39]. The particle morphology of the intermetallic particles exhibits either a more globular shape with a particle diameter of less than 5 μm or larger elongated particles with a length of several

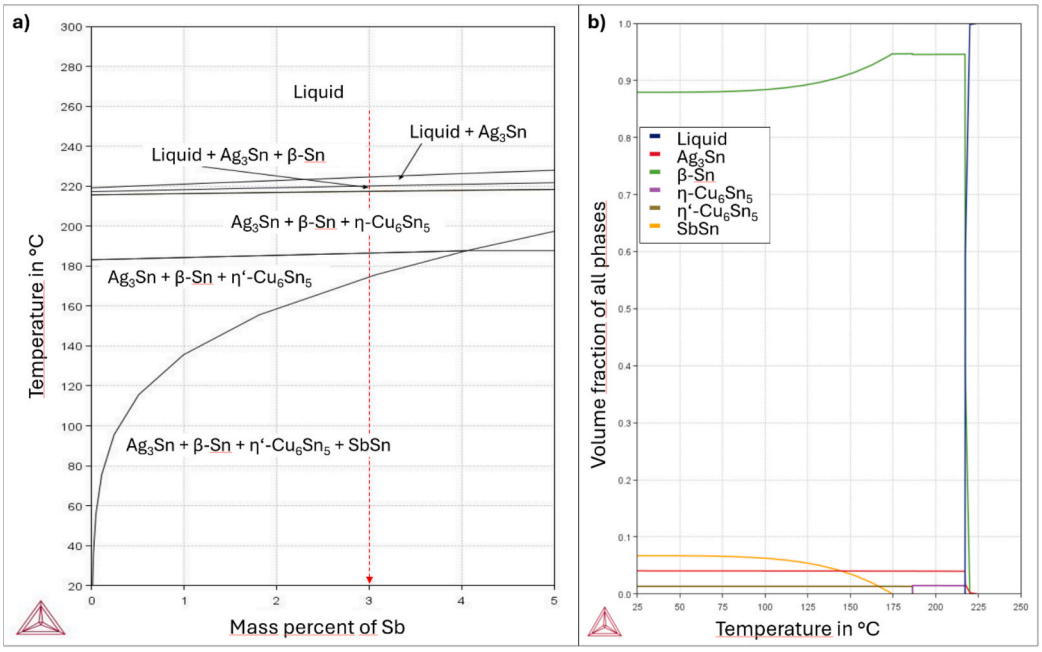

Fig. 1. Phase diagram simulation of SAC 396+, a) Equilibrium Sn-Sb phase diagram at 3.9 % Ag and 0.6 % Cu with varying Sb content, b) Volume fraction of stable phases between room temperature and melting temperature.

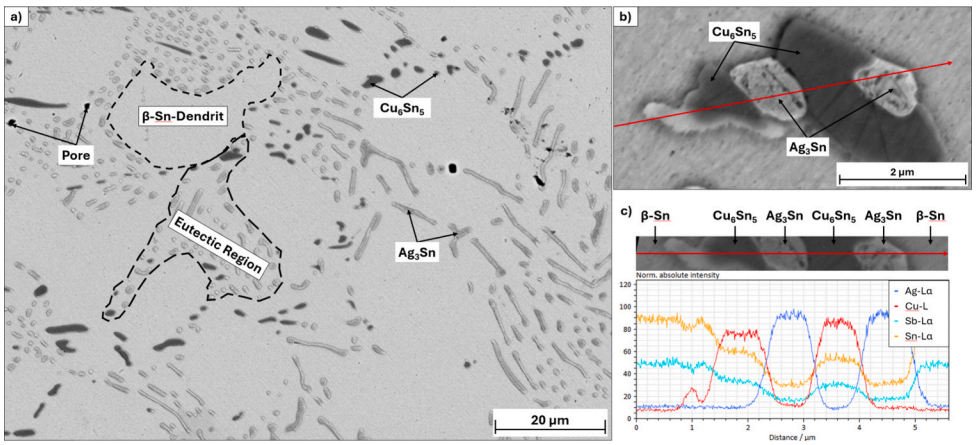

Fig. 2. BSE-SEM overview of SAC 396 + after casting and pre-ageing for 24 h at 125 °C, a) overview of β-Sn-dendrites, which are fully surrounded by eutectic regions, b) Ag_3Sn and Cu_6Sn_5 particles sharing a phase boundary, c) corresponding EDS line scan.

micrometers. Thereby, the elongation of the Ag_3Sn-particles is more pronounced than of the η'-Cu_6Sn_5-particles. It could be found that some of the Ag_3Sn- and Cu_6Sn_5-particles share a phase boundary with each other (Fig. 2-*b*). These Cu_6Sn_5-particles show brighter areas at the edge of the particle, and a corresponding EDS line scan reveals a higher concentration of Sb in the edge of the Cu-particle than in the core with a decreasing tendency towards the particle core (Fig. 2-*c*). A qualitative comparison of the Sb concentration across these particles shows the highest concentration plateau of Sb in β-Sn, the second highest plateau in Cu_6Sn_5 and the lowest concentration plateau of Sb in the Ag_3Sn particle phase. However, regarding the Thermo-Calc simulations in Table 2, the low temperature η'-Cu_6Sn_5 phase does not dissolve any Sb at temperatures between 25 °C and 180 °C in equilibrium, whereas the high temperature η-Cu_6Sn_5 phase dissolves a slight amount of Sb at 190 °C. High temperature η-Cu_6Sn_5 particles may have formed by heterogeneous nucleation on the already existing Ag_3Sn particle in the liquid phase. Consequently, the transformation of these η-Cu_6Sn_5 particles into η'-Cu_6Sn_5 (low temperature), which is the stable phase below 186.5 °C, via solid-state reaction may not have occured due to the relatively high cooling rate of the material in the casting mold. According to literature, the hexagonal high temperature η-Cu_6Sn_5 phase could be stabilized at temperatures below 186 °C or even at room temperature by adding Sb, which leads to the formation of $Cu_6Sn_{5-x}Sb_x$ [40,41].

Fig. 3-a shows a dendritic region, where some small, darker particles with diameters of less than 1 µm and with a tendency towards an angular particle shape were found in β-Sn. An EDS measurement (Fig. 3-b) of these reveals a higher concentration of 17.96 at.-% and 20.03 at.-% of Sb in these darker particles than in the brighter surrounding β-Sn-matrix with 3.98 at.-% and 5.00 at.-%. Furthermore, a low concentration of Ag with around 3 at.-% was found in these particles and also in the surrounding β-Sn, and a low concentration of Cu with around 2 at.-% was found only in β-Sn, which could both be the case due to broader width of the electron interaction volume. An EDS-line-scan of a β-Sn-dendrite-particle (Fig. 4-a and −b) also reveals a higher concentration of Sb in these darker particles than in the brighter surrounding β-Sn-matrix. Furthermore, as can be seen from the line scan in Fig. 4-b, Cu and Ag in the particles remain on the same concentration level as in the surrounding matrix, which rules out the possibility that these particles are Ag_3Sn or Cu_6Sn_5. Both facts are an indication for the occurence of SbSn-particles. It must be noted that, due to the size of the interaction volume, an exact chemical composition cannot be determined by EDS analysis. For this reason, XRD measurements were performed (Fig. 6). Wang et al. [42] found in Sn-3.4Ag-0.8Cu-5Bi-7Sb-0.05Ni also darker particles inside dendritic β-Sn, which were identified as SbSn. For SbSn, Belyakov et al. [28] postulated an orientation relationship of $(100)_{\beta Sn} \,||\, (100)_{SbSn}$ with $[001]_{\beta\text{-}Sn} \,||\, [001]_{SbSn}$.

Although Sb is a slightly heavier element with 121.76 g/mol [39] than Sn with 118.71 g/mol [39] and their average atomic number is with $\overline{Z} = 50.5$ slightly larger compared to $Z = 50$ of Sn, the difference in Z-contrast is relatively small and other effects could overlay the material contrast [43,44]. Especially for small working distances (WD < 10 mm), low acceleration voltages, and for non-planar surfaces with a distinct topography, there could be a topography effect [45]. This edge effect together with the effect that the interaction volume in these small particles is minor in comparison to the surrounding matrix lead to less back scattered electrons from the particle, and could result in a darker appearance than the surrounding matrix [45].

Table 2
CALPHAD calculations of the mass fraction of Sb in each phase at various temperatures. The symbol * means that the corresponding phase is not existing at this temperature.

Temperature	Mass fraction of Sb in the corresponding phase				
	β-Sn	**SbSn**	**η-Cu_6Sn_5**	**η'-Cu_6Sn_5**	**Ag_3Sn**
25 °C	8.00E-05	4.85E-01	*	0	1.16E-03
35 °C	1.50E-04	4.83E-01	*	0	1.25E-03
50 °C	3.30E-04	4.81E-01	*	0	1.37E-03
100 °C	3.02E-03	4.72E-01	*	0	1.70E-03
125 °C	7.46E-03	4.67E-01	*	0	1.85E-03
150 °C	1.65E-02	4.64E-01	*	0	2.03E-03
160 °C	2.19E-02	4.62E-01	*	0	2.13E-03
170 °C	2.86E-02	4.61E-01	*	0	2.24E-03
180 °C	3.21E-02	*	*	0	2.10E-03
190 °C	3.21E-02	*	2.76E-07	*	1.79E-03

3.1.3. *TEM investigation of β-Sn*

A TEM selected area electron diffraction (SAED) image of a tip, which was prepared with Focus Ion Beam method of near-eutectic β-Sn, shows the characteristic crystal structure of the I41/amd cell (Fig. 5). Some crystallographic planes were detected, and the related calculated inter-atomic distances are shown in Table 3 and compared to literature values of β-Sn [46].

It can be stated that there is an increase in lattice parameters with an average lattice expansion of 0.92 %, due to introduction of the solid solution of Sb in the β-Sn-matrix (Table 3).

3.1.4. *XRD measurements*

An XRD-profile of SAC 396+, measured between 30°2θ and 100°2θ is shown in Fig. 6-*a*, and measured between 30°2θ and 50°2θ is shown in Fig. 6-*b*. The expected three main phases in SAC 396 + Sn_1, η'-Cu_6Sn_5 and Ag_3Sn have the same crystal structure as in alloy SAC 387 (Table 4). In addition to the expected Sn-Ag-Cu-phases, two Sb-containing phases

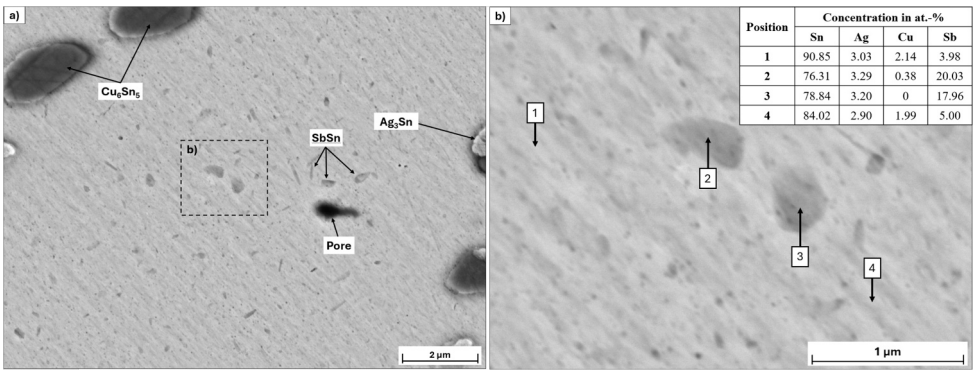

Position	Concentration in at.-%			
	Sn	Ag	Cu	Sb
1	90.85	3.03	2.14	3.98
2	76.31	3.29	0.38	20.03
3	78.84	3.20	0	17.96
4	84.02	2.90	1.99	5.00

Fig. 3. a) BSE-SEM overview of a dendritic region, b) EDX analysis of SbSn particles in β-Sn.

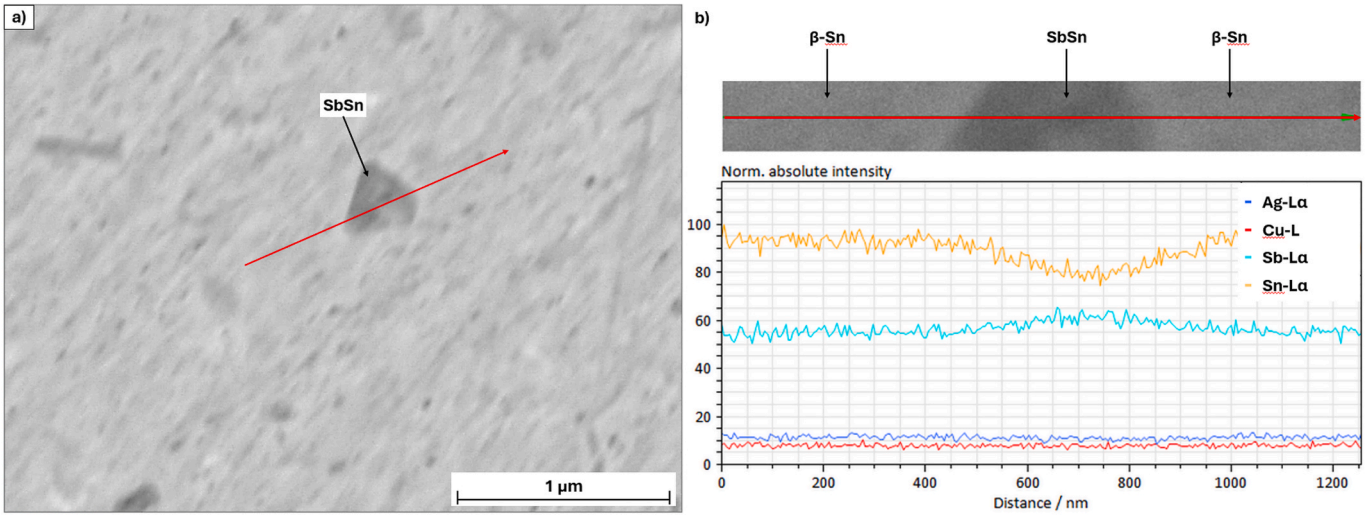

Fig. 4. a) BSE-SEM image of a SbSn particle in β-Sn, b) corresponding EDS line scan.

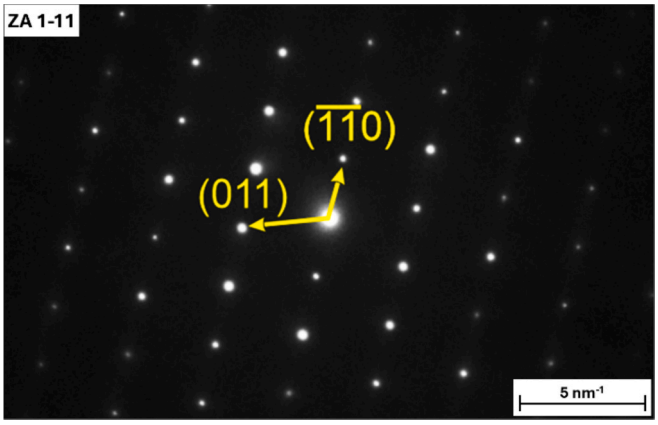

Fig. 5. TEM SAED image of a near-eutectic β-Sn dendritic region and detected lattice planes.

were detected, which are on the one hand Sb_2Sn_{23}, which crystallizes in the same tetragonal I41/amd crystal cell as β-Sn (Sn_1) and shares the same peaks in the XRD profile, and on the other hand $Sb_{0.49}Sn_{0.51}$, which crystalizes in a R-3 m hexagonal crystal cell. Since Sb has been reported to be homogeneously distributed within the β-Sn matrix [2], as also confirmed by the TEM investigations conducted in this study (Table 3), the Sb_2Sn_{23} phase can be interpreted as a β-Sn-based matrix containing incorporated Sb atoms. This interpretation is further supported by the coincidence of the Sb_2Sn_{23} diffraction peaks with those assigned to the Sn1 phase in SAC 387 (Fig. 7). A peak shift of the main β-Sn peaks towards smaller angles occurs with Sb addition, due to an increase in lattice parameter. *Wolcyrz et al.* [46] obtained lattice parameters of a = b = 5.8308 Å and c = 3.1810 Å for β-Sn (Sn_1), whereas *Raynor and Lee et al.* [47] stated lattice parameters of a = b = 5.8460 Å and c = 3.1810 Å for β-Sn with introduced Sb atoms (Sb_2Sn_{23}), which means an increase of 0.0152 Å or $1.52 \cdot 10^4$ pm in a- and b-direction, whereas the lattice parameter in c-direction remains constant. In literature, Sb_2Sn_{23} was hardly found in Sn-Ag-Cu alloys with Sb addition. Nonetheless, low pressure cold spraying of Sn-Sb-Cu based Babbitt alloys on AISI 1045 steel substrates resulted in the formation of Sb_2Sn_{23} [40]. The SbSn phase $Sb_{0.49}Sn_{0.51}$ was found by *Norén et al.* and *Schmetterer et al.* [37,48].

3.1.5. EBSD mapping of cross sections

The Young's modulus values of β-Sn (I41/amd), calculated by *Ernst et al.* [31], were 66.8 ± 0.1 GPa in <001>, 62.8 ± 0.5 GPa in <110>, and 23.3 ± 0 GPa in <100>, with a maximum difference of 43.6 GPa [31]. Thus, a selection of evaluated crystal structures and crystal orientations in the cross sections of the creep samples, measured with EBSD, is shown in Fig. 8. The first solidified section in the cast rod, respectively the lower part in the gating system, exhibits a larger number of grains with a variety of crystal orientations, whereby a <110>- crystal orientation is present in this section (Fig. 8-a to −d). In contrast, the higher sections in the gating system, which solidified later in the casting process, show only a few grains with a crystallographic

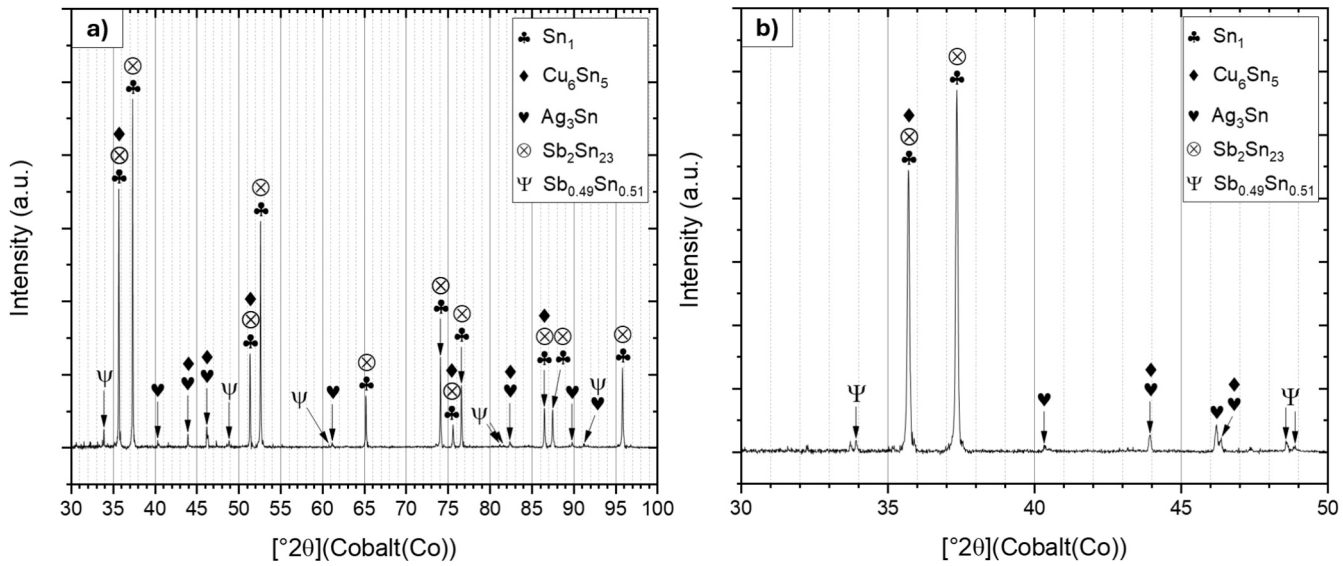

Fig. 6. XRD profiles of SAC 396+, pre-aged for 24 h at 125 °C, a) overview in the angle range between 30°2θ and 100°2θ, b) detailed view, in the angle range between 30°2θ and 50°2θ.

Table 3
Calculated inter-atomic distances of near-eutectic β-Sn, corresponding to the SAED image of Fig. 5 and compared to literature values [46].

Indices	*Calculated inter-atomic distances in nm*	*Inter-atomic distances in nm* [46]	*Lattice expansion*
$0\bar{1}\bar{1}$	0.28421	0.27925	**1.78 %**
$\bar{1}2\bar{1}$	0.20446	0.20166	**1.39 %**
$\bar{1}\bar{1}0$	0.20597	0.20615	**−0.09 %**
$\bar{1}0\bar{1}$	0.28090	0.27925	**0.59 %**

Table 4
Evaluated phases of SAC 387 and SAC 396+, and their corresponding crystal cells.

Symbol	SAC 387	SAC 396+
♣	Sn_1 (tetragonal, I41/amd)	Sn_1 (tetragonal, I41/amd)
◆	η'-Cu_6Sn_5 (monoclinic, C12/c1)	η'-Cu_6Sn_5 (monoclinic, C12/c1)
♥	Ag_3Sn (orthorhombic Pmmn)	Ag_3Sn (orthorhombic, Pmmn)
⊗	–	Sb_2Sn_{23} (tetragonal, I41/amd)
Ψ	–	$Sb_{0.49}Sn_{0.51}$ (rhombohedral, R-3 m)

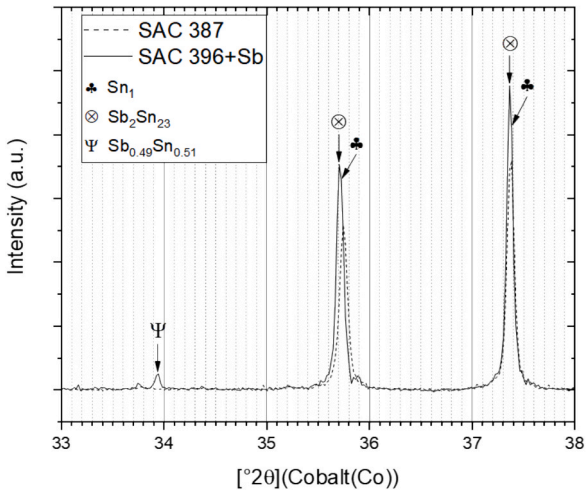

Fig. 7. Main peaks of SAC 396 + vs. SAC 387 in the angle range between 33°2θ and 38°2θ.

orientation mainly oriented in <110> -direction (Fig. 8-*d, −e)*. Sometimes even a single crystalline structure is present. This leads to the conclusion that <110> -grains overgrow other oriented grains and <110> is the dominating crystal orientation. For the actual creep experiments, only samples of higher sections in the gating system were used for creep testing to minimize the influence of crystal orientation on the creep results.

3.2. Compression creep behavior

3.2.1. Creep-strain vs. creep time curves of SAC 396+

The measured creep-strain vs. creep-time plots of SAC 396 + creep samples, pre-aged at 125 °C for 24 h and tested at 35 °C, 85 °C and 125 °C are shown in Fig. 9-*a, −b,* and *−c*. The curves for 50 °C and 100 °C were omitted for clarity. Generally, the curvature of the region of transition from primary creep to secondary creep is more pronounced, if the stresses are higher. In detail, at temperatures of 35 °C, 85 °C and 125 °C, as well as stresses lower than 30 MPa, the primary creep state is not incisive, and the samples already reach the secondary creep regime after a short time. In Fig. 10-*a, −b* and *−c*, the creep-strain vs. creep-time curves of long-term pre-aged samples, which were pre-aged for 24 h, 500 h or 1500 h each at 125 °C are shown, which were all compression creep tested at 50 °C. The corresponding true creep strain rate vs. creep-time plots for SAC 396+, which were condensed and smoothed by using a Savitzky-Golay filter to limit the influence of noise, are shown in Fig. 9-*d, −e, −f* and Fig. 10-*d, −e, −f*. At each test temperature and for longer pre-ageing times, increasing the initial stress causes the material to enter the secondary (quasi steady state) creep regime at lower true creep strain values.

3.2.2. Norton-plot and Arrhenius curves

In Fig. 11-*a*, the evaluated true minimum creep strain rates are plotted against the determined true stresses in a Norton Plot diagram. Between 35 °C and 100 °C, the slope of these curves and the stress exponent remain constant at 7.4 and 7.5, whereas at 125 °C, the stress exponent is lower with 4.8. A stress exponent of n = 3 means viscous glide of dislocations by dragging solute atoms (Class A / Class I), n = 5 means dislocation climb, achieved by lattice diffusion or achieved by dislocation pipe diffusion at n = 7 (Class M / Class II) [49]. Regarding the microstructure, for Class A, the dislocations are rather uniformly

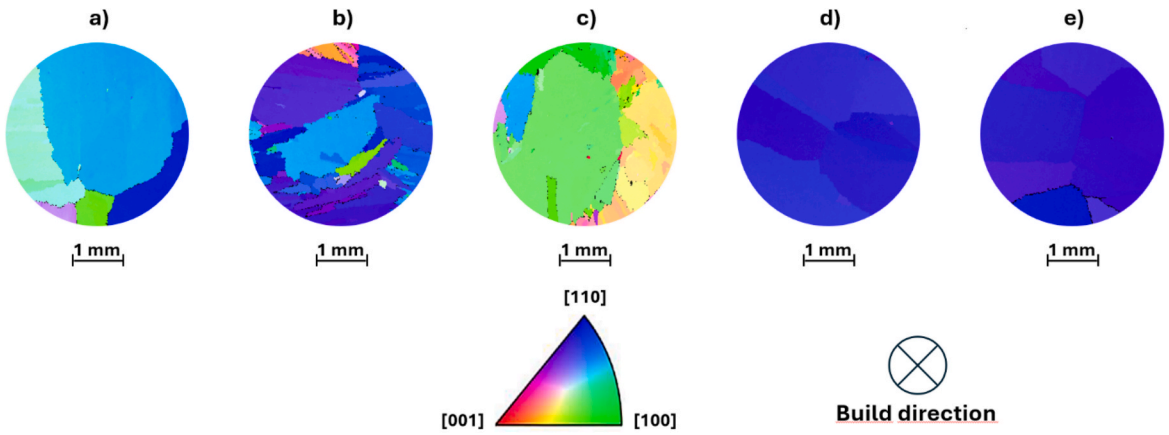

Fig. 8. EBSD mapping of cross sections of selected creep samples, a), b), c) first solidified section in a casting rod, d) and e) later solidified sections during the casting process.

distributed and there should be no subgrain formation, whereas in Class M, a heterogeneous subgrain structure is postulated, with larger dislocation free areas, which are surrounded by loose-knit subgrain boundaries [50–53]. The change in slope from 100 °C to 125 °C leads to the assumption that a change in dislocation creep mechanism occurs slightly above 100 °C. In Literature, for Sn-1.0Ag-0.5Cu (SAC 105) and Sn-3.0Ag-0.5Cu (SAC 305) a transition was found at 150 °C, whereas at lower temperatures, dislocation climb controlled by pipe diffusion is dominating (n = 7), and at higher temperatures, dislocation climb controlled by lattice diffusion (n = 5) is the dominating creep mechanism [33]. For binary Sn-Sb-alloys, this transition was described at around 100 °C [23]. This leads to the assumption that above 100 °C dislocation recovery is more pronounced with a decreasing dislocation density and therefore less dislocation pipe diffusion. The change in stress exponent at a temperature of 35 °C from 7.4 at high stresses to 3.0 at low stresses (Fig. 11-*a*), indicate a mechanism change from Class M to Class A behavior [49,53]. The critical stress, at which the gliding dislocation breaks away from its solute atom atmosphere and the stress exponent transfers from 3 to 5 or 7 [49] was in literature evaluated for alloy Sn-3.4Ag-0.7Cu-3.2Bi-3.0Sb-Ni-x at 25 MPa, which is equivalent to Fig. 11-*a* [54].

By comparing the Norton-Plot curves of 24 h, 500 h, and 1500 h at 125 °C pre-aged samples (Fig. 11-*b*), it is noticeable that with increasing isothermal ageing from 24 to 500 h or 1500 h, the Norton-Plot curves are shifted towards smaller stresses, indicating a decrease in creep resistance with increasing isothermal ageing. The stress exponent of the 500 h pre-aged samples is 7.3 and is equivalent to the 24 h pre-aged samples, whereas the 1500 h pre-aged samples show a slight increase in stress exponent with a value of 8.0. Analyzing the interparticle spacing of Ag_3Sn and Cu_6Sn_5 in SAC 396 + at three ageing conditions (Table 7), the median value of the 24 h at 125 °C pre-aged sample is 4.18 μm and was calculated from 3583 measured interparticle distances, whereas the median value after 500 h at 125 °C is 5.17 μm, calculated from 2662 measured distances, and after 1500 h at 125 °C is 7.86 μm, and was calculated from 1739 interparticle distances. Despite the fact, that an increase between 500 h and 1500 h of 2,69 μm occurs, the creep resistance seems to be quite unaffected, which could be the result of solid solution and precipitation hardening by Sb.

In Table 5 literature values of different creep tested Sn-Ag-Cu alloys are shown. Mathew *et al.* [55] researched the creep behavior of pure tin between 23 °C and 150 °C and postulated a stress exponent of 7.6, associated with dislocation climb controlled by lattice diffusion [55]. The stress exponent values for different SAC-base alloys like SAC 105, SAC 387, Sn-3.9Ag-0.6 Cu (SAC 396), and Sn-4.0Ag-0.5Cu (SAC 405) were in the range between 3.8 and 7, which was generally associated with dislocation creep [33,56–60]. Also, there is subdivision into a high-stress (n ~ 7–12) and a low-stress (n ~ 3–6) regime described for Sn-3.0Ag-0.5Cu (SAC 305) [61]. However, it was found that the addition of Sb alone or in combination with other additional alloying elements led to an increase in stress exponent. For example, the addition of 0.5 wt-% Sb to SAC 105 led to slightly higher stress exponent values of 7.2–9.3 compared to pure SAC 105 alloy with a value in the range of 5.3–7.0, whereby the creep mechanism was identified as dislocation climb, which was controlled by pipe diffusion [58].

For evaluating the activation energies, Arrhenius plots were generated from creep strain rates at the same initial stresses and from three different temperatures. As can be seen in Fig. 12, an increase in initial stress leads to a decrease in activation energy, whereby there is a measurement inaccuracy due to trend lines being drawn of only two values. At a low stress of 12.5 MPa and temperatures of 85 °C, 100 °C, and 125 °C, one of the three data points show a deviation from the original regression line, which could be the case due to a mechanism change in dislocation creep mechanism between 100 °C (controlled by pipe diffusion) and 125 °C (controlled by lattice diffusion) or be the case due to enhanced coarsening of intermetallic particles (Fig. 12). An equivalent behavior with similar values in the temperature range between 90 °C and 160 °C could be found in literature for polycrystalline, whereby the different slopes are associated with a high-temperature-regime (Q ~ 108.8 kJ/mol) and a low-temperature-regime (Q ~ 46 kJ/mol) [63]. Moreover, the values of Q = 100 kJ/mol with n = 5 are associated with dislocation climb, controlled by lattice diffusion, and Q = 55 kJ/mol with n = 7, which is associated with dislocation climb, controlled by pipe diffusion [33]. Furthermore, it is described in literature that both mechanism, dislocation pipe diffusion and lattice diffusion, could occur simultaneously, which is associated with Q ~ 83.6 kJ/mol [64].

For a better comparison, the evaluated activation energies are plotted in Table 6. The values correspond to *Song et al.* [61], which found activation energies of 95 kJ/mol (low stress regime) and 75 kJ/mol (high-stress regime) [61].

3.2.3. *Microstructure after compression creep of alloy SAC 396+*

In Fig. 13-*b*, the microstructure of a sample creep tested at 100 °C with an initial stress of 20 MPa is shown, which has undergone a true creep strain of 13.1 %. It is compared to a sample before creep testing, which was pre-aged for 24 h at 125 °C (Fig. 13-*a*), where it could be seen that after compression creep testing, the elongated Ag_3Sn and Cu_6Sn_5 particles are much smaller and exhibit a more globular shape. In Fig. 13-*a*, there are also a higher number of small SbSn particles (~ 0.5 μm) in the dendritic region, whereas after creep testing, there are less SbSn particles in the dendritic region, but one larger SbSn particle with approximately 5 μm could be found in the eutectic region between

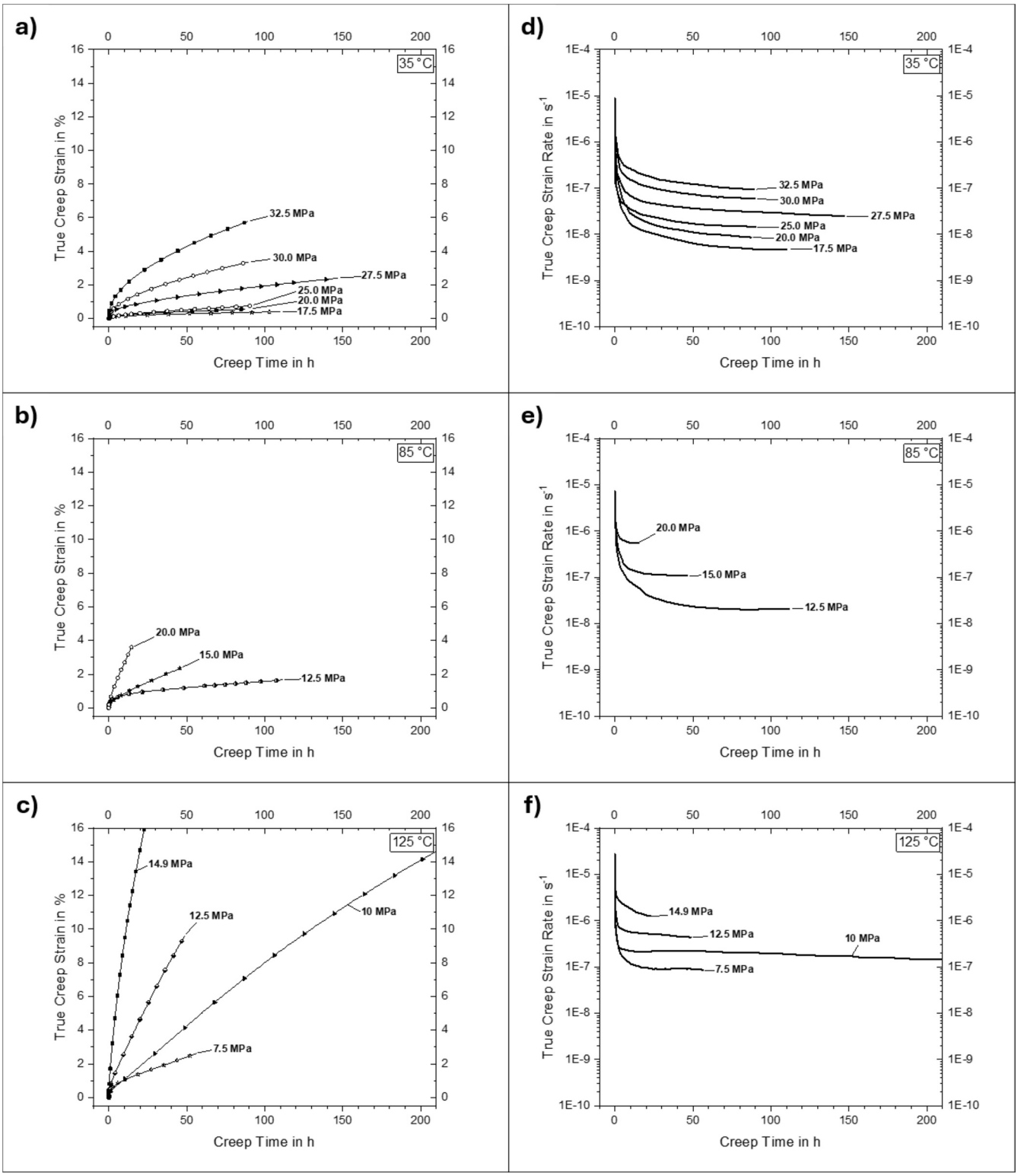

Fig. 9. Creep-Strain vs. Creep-Time curves of pre-aged (24 h/125 °C) samples, tested at a) 35 °C, b) 85 °C, c) 125 °C, and Strain-Rate vs. Creep-Time curves of e) 35 °C, e) 85 °C, f) 125 °C.

globular Ag_3Sn particles (Fig. 13-*b* and Fig. 14). Despite the fact that the partition coefficient of Sb shows a value of around k ~ 1.2 and is greater than 1 [28], the Sb concentration and therefore SbSn volume fraction should be higher in the first solidifying dendritic region. But in literature, the occurrence of larger SbSn-particles in the eutectic region is also postulated and associated with a larger interfacial energy of SbSn-particles that nucleate on Cu_6Sn_5 compared to cuboidal SbSn-particles inside the β-Sn-dendrites [28]. The higher coarsening rate of possible SbSn in the eutectic region may also lead to larger SbSn precipitates at the phase boundaries of Ag_3Sn particles.

Furthermore, EBSD mappings of Inverse-Poly-Figures in y-direction (IPFY) of longitudinal cross sections are compared to each other in

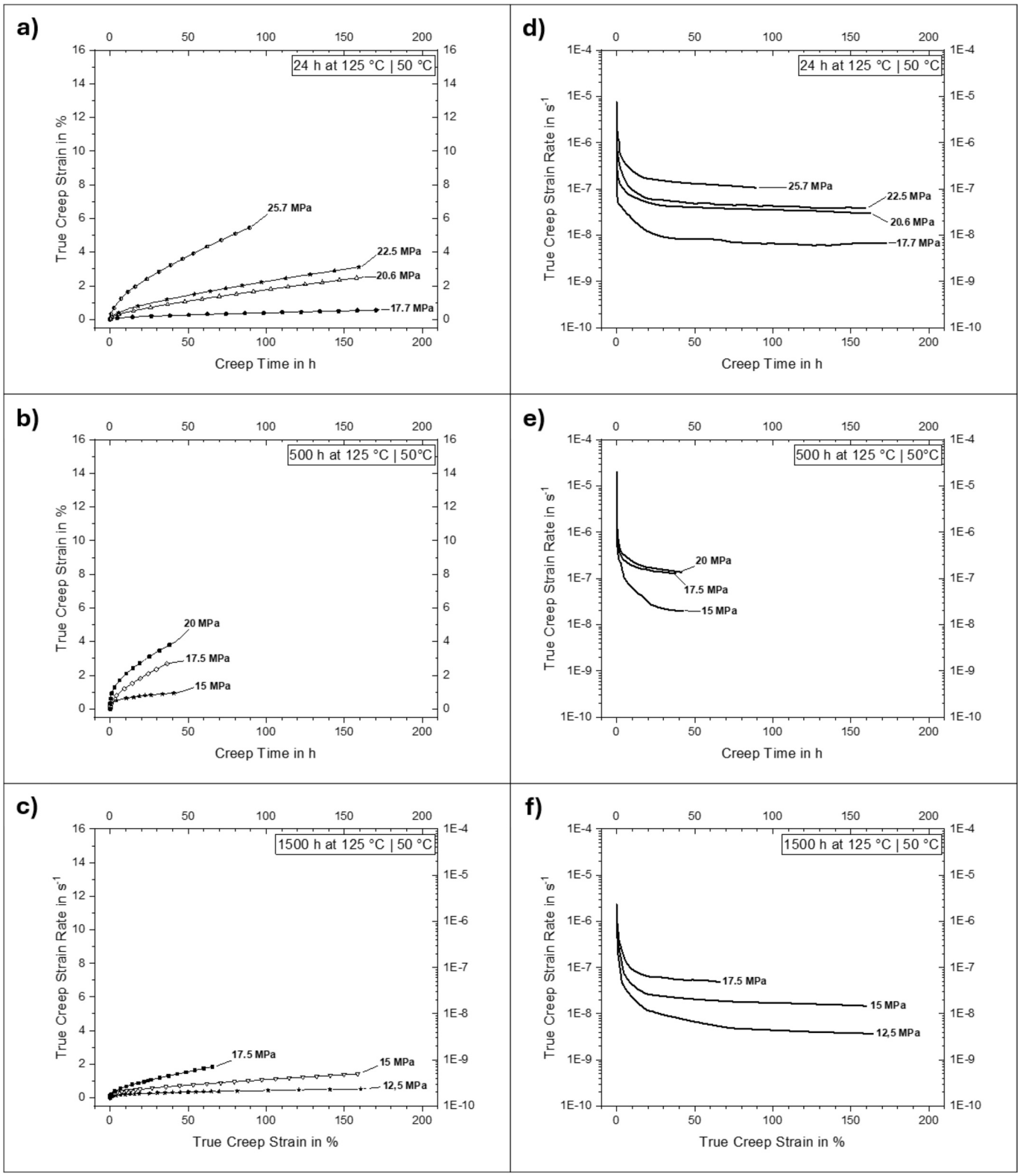

Fig. 10. Creep-Strain vs. Creep-Time curves of samples, which were creep tested at 50 °C and pre-aged at 125 °C for a) 24 h, b) 500 h, and c) 1500 h, as well as corresponding True-Creep-Strain-Rate vs. Creep-Time curves: d) 24 h/125 °C, e) 500 h/125 °C, and f) 1500 h/125 °C.

Fig. 15-*a, −b, −c*, as well as Grain Average Misorientation (GAM) maps in Fig. 15-*d, −e, −f*, which visualize the plastic strain, one grain has undergone in comparison to its neighbor grains [65]. The top edge of the image corresponds to one of the front surfaces of the creep sample. The number of grains vary with no clear tendency throughout the three temperatures. In all three samples, grain boundaries were found, which are mainly oriented in 45° or perpendicular to the load axis. These grain boundaries exhibit a significant number of pores, whereas the number of pores increases with testing temperature. Consequently, there may have occurred some slight grain boundary slipping at 100 °C. It can be found

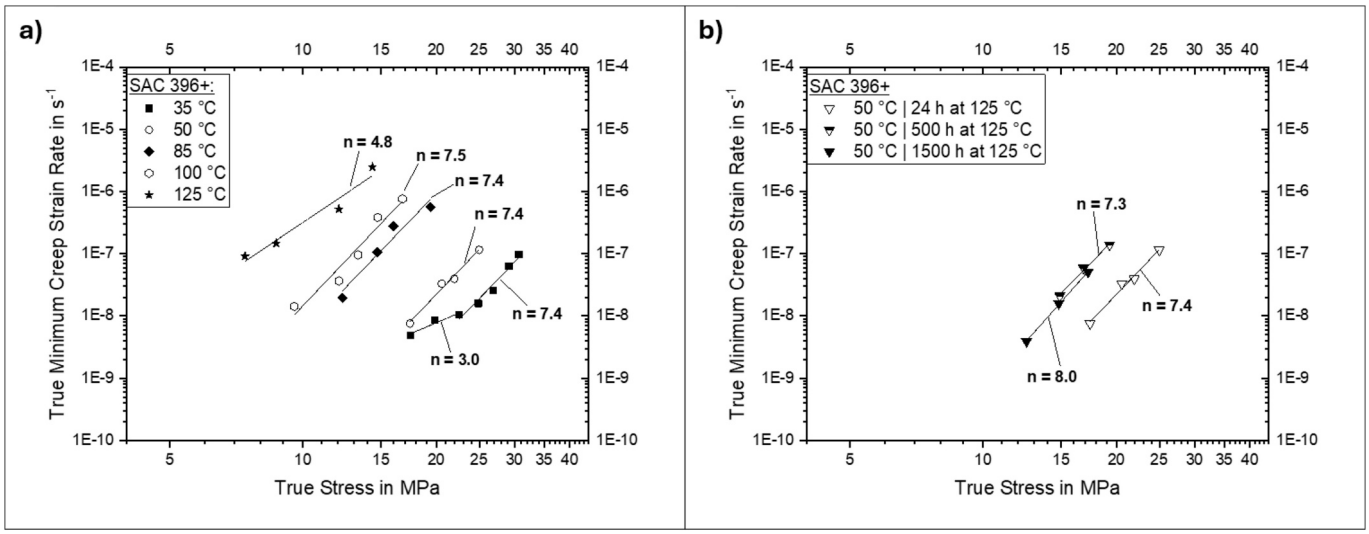

Fig. 11. Norton-Plot diagrams of compression creep tested SAC 396+, a) at temperatures of 35 °C, 50 °C, 85 °C, 100 °C and 125 °C, b) of pre-aged samples, tested at 50 °C.

Table 5
Postulated stress exponent and activation energy values by various authors.

Material	Testing Condition	T (°C)	σ (MPa)	n	Qc (kJ/mol)	Creep mechanism	Ref.
Pure Sn	Tensile Creep	23–150	1–30	7.6 ± 0.2	60.3 ± 3.8	Dislocation climb controlled by lattice diffusion	[55]
Sn-5Sb	Tensile Creep	23–200	1–30	5.0 ± 0.3	44.7 ± 3.7	Viscous glide controlled by pipe diffusion	[55]
Sn-1.0Ag-0.5Cu (SAC 105)	Compression Creep	60–150 150–200	7–14	7 5	55 100	Dislocation climb controlled by dislocation pipe diffusion (T < 150 °C) and by lattice diffusion (T > 150 °C)	[33]
SAC 105	Tensile Creep	25 70 110	14–30	7.0 6.0 5.3	40.7	Dislocation climb controlled by pipe diffusion	[58]
SAC 105 + 0.5 wt-% Sb	Tensile Creep	25 70 110	14–30	9.3 8.0 7.2	54.4	Dislocation climb controlled by pipe diffusion	[58]
Sn-3.0Ag-0.5Cu (SAC 305)	Compression Creep	60–150 150–200	7–14	7 5	55 100	Dislocation climb controlled by dislocation pipe diffusion (T < 150 °C) and by lattice diffusion (T > 150 °C)	[33]
SAC 387	Tensile Creep	75	12–27	17	–	–	[62]
Sn-3.9Ag-0.6Cu (SAC 396)	Compression Creep	−25–75 75–160	6.5–40.3 2.7–9.8	3.2 (low stress) & 4.9 (high stress) 4.2 (low stress) & 5.0 (high stress)	25 ± 7 (< 75 °C) 95 ± 14 (75-160 °C)	Grain boundary diffusion at low temperatures and dislocation creep with lattice or bulk diffusion at high temperatures	[57]

that the <110> crystal orientation is dominating at all three temperatures, which is in accordance with literature, where it was found that the dominant slip system is (1–10)[001] [66].

GAM-investigations showed that a relatively larger grain deformation (green color) occurs in perpendicular oriented grains (Fig. 15-*c*), in grains, oriented in [001] (Fig. 15-*d*) or in grains, which are oriented in near-[001] crystal orientation (Fig. 15-*e*).

3.2.4. Comparison of creep behavior of SAC 396 + with SAC 387

Comparing the microstructure of SAC 396+ and near-eutectic SAC 387 (Fig. 16), SAC 387 has a higher volume fraction of eutectic region with 83.2 vol-% than SAC 396+ with 56.7 vol-%. Evaluating the eutectic region, the median value of the particle size and interparticle spacing of Ag_3Sn and Cu_6Sn_5 increases from the as cast condition with increasing ageing time from 24 h to 1500 h at 125 °C (Table 7). The median particle size in SAC 387 exhibits in the as cast condition 0.38 μm and after 1500 h at 125 °C 0.63 μm, which means an increase of 0.24 μm, whereas the interparticle spacing increases from 2.91 μm to 4.95 μm, which means a difference of 2.04 μm. Regarding SAC 396+, the median particle size increases from as cast (0.67 μm) to 1500 h / 24 h (1.11 μm), which means an increase of 0.44 μm with is larger than in SAC 387. There is also a larger increase in interparticle spacing with 5.11 μm compared to SAC 387. In basic SAC alloys, creep is primarily controlled by particle size and interparticle spacing [6]. Nonetheless, the creep performance of Sb containing SAC 396+ is at all testing temperatures and ageing conditions better than of SAC 387 (Fig. 16) due to solid solution hardening and SbSn particle hardening. For a clearer comparison of the loss in strengthening due to coarsening of Ag_3Sn- und Cu_6Sn_5-particles, the Orowan stress was calculated, using the following *equation (1)* [67] and the calculated stresses are shown in Table 7:

$$\sigma_{Or} = \frac{0.84 \bullet M \bullet G \bullet b}{\lambda - 2r} \quad (1)$$

Here, $M = 3$ is the Taylor factor, $2r$ is the median diameter of the particles and λ describes the distance between the particles [67]. For the burgers vector b, the value for the {110} < 001 > slip family was used, which is 0.32 nm [68,69]. The shear modulus G was calculated for 50 °C to correspond with the creep experiments of pre-aged specimens, using the temperature dependent *equation (2)*, proposed by *Kanjilal et al.* [33]:

$$G(MPa) = 20632 - 37.67 \bullet T(^{\circ}C) \quad (2)$$

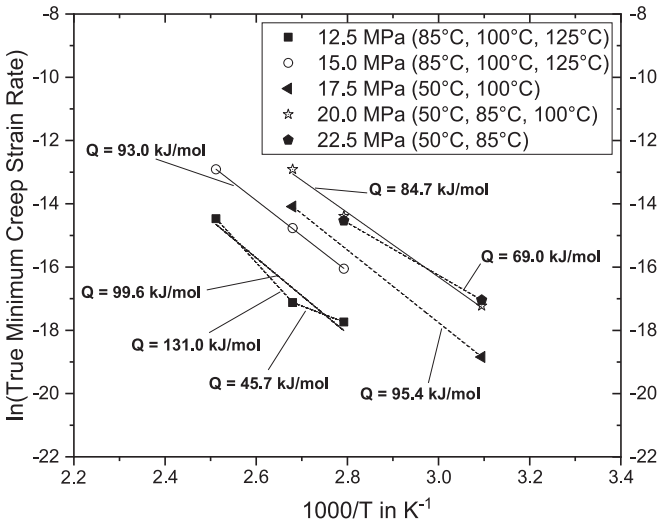

Fig. 12. Arrhenius plots and calculated activation energies for stresses of 12.5 MPa, 15 MPa, 17.5 MPa, 20 MPa, and 22.5 MPa.

Table 6
Evaluated activation energy values for different initial stresses. The values, which were obtained by interpolating data points in Fig. 12, are charted in brackets.

Test temperature	*12.5 MPa*	*15 MPa*	*17.5 MPa*	*20 MPa*	*22.5 MPa*
35 °C, 50 °C, 85 °C	–	–	–	–	*(69.0 kJ/mol)*
50 °C, 85 °C, 100 °C	–	–	*(95.4 kJ/mol)*	*84.7 kJ/mol*	–
85 °C, 100 °C, 125 °C	*99.6 kJ/mol (45.7 kJ/mol, 131.0 kJ/mol)*	*93.0 kJ/mol*	–	–	

As can be seen in Table 7, the Orowan stress of eutectic Ag_3Sn and Cu_6Sn_5 particles in alloy SAC 396 + decreases more significantly with ageing from 7.27 MPa in the as cast condition to 2.24 MPa after pre-ageing for 1500 h at 125 °C in comparison to SAC 387 from 5.98 MPa in the as cast condition to 3.50 MPa after long-term ageing. The calculated Orowan stresses for the dendritic SbSn particles, which are also existing in the eutectic region, are 5.46 MPa after 24 h at 125 °C and 4.07 MPa after 500 h at 125 °C and are therefore of the same order of magnitude as those associated with Ag_3Sn and Cu_6Sn_5. Despite the slightly higher silver content of SAC 396+ and the more strongly decreasing Orowan strengthening contribution of Ag_3Sn, SAC 396+ exhibits consistently higher creep strength than SAC 387 at all investigated temperatures and ageing conditions, what provide strong evidence that the addition of Sb makes a substantial contribution to the enhanced creep resistance of SAC 396+ .

At a test temperature of 35 °C (Fig. 17-*a*), SAC 387 shows a higher stress exponent in the dislocation creep regime with 12.1 than SAC 396+ with 7.4, which results from a higher stress sensitivity due to smaller interparticle spacing of SAC 387. At a test temperature of 85 °C (Fig. 17-*c*) and 100 °C (Fig. 17-*d*), the trend reversed and SAC 387 shows a lower stress exponent and stress sensitivity with 5.7 and 5.1 than SAC 396+ with 7.4 and 7.5, which could be due to SbSn particle hardening. At 125 °C in Fig. 17-*e*, despite the regression line of SAC 387, the measured data points show a clear trend towards a strong increase of the curve, indicating a power-law-breakdown behavior. Regarding the effect of isothermal ageing on the microstructure (Table 7) and creep behavior (Fig. 16 and Fig. 17-*f*), a longer pre-ageing time of 500 h or 1500 h at 125 °C instead of 24 h at 125 °C led to an increase in interparticle spacing in SAC 387 from 3.79 µm (24 h) to 4.40 µm (500 h) and to 4.95 (1500 h) µm and in SAC 396+ from 4.18 µm (24 h) to 5.17 µm (500 h) and to 7.86 µm (1500 h), whereas the curves of SAC 387 are shifted towards smaller stresses, indicating a lower creep resistance. While the stress exponent values of SAC 396+ remain more or less constant between 7.4 and 8.0, the stress exponent of SAC 387 increased significantly from 8.4 to 21.4, indicating a power-law-breakdown behavior (Table 8).

Table 7
Particle size and interparticle spacing of Ag_3Sn and Cu_6Sn_5 particles in SAC 387 and SAC 396+, each after casting and after pre-ageing at 125 °C for 24 h, 500 h, or 1500 h, as well as the number of the measured particles in columns. The calculated Orowan stresses, using equation (1) were also added.

Isothermal Ageing Condition	SAC 387			SAC 396+		
	Median Particle Size in µm	Median Interparticle Spacing in µm	Orowan Stress at 50 °C in MPa	Median Particle Size in µm	Median Interparticle Spacing in µm	Orowan Stress at 50 °C in MPa
As cast	0.38 (4316)	2.91 (5440)	5.98	0.67 (6785)	2.75 (5708)	7.27
24 h at 125 °C	0.30 (4362)	3.79 (4453)	4.33	0.84 (4645)	4.18 (3583)	4.53
500 h at 125 °C	0.43 (4392)	4.40 (2710)	3.81	0.71 (4556)	5.17 (2662)	3.39
1500 h at 125 °C	0.63 (4454)	4.95 (2605)	3.50	1.11 (2276)	7.86 (1739)	2.24

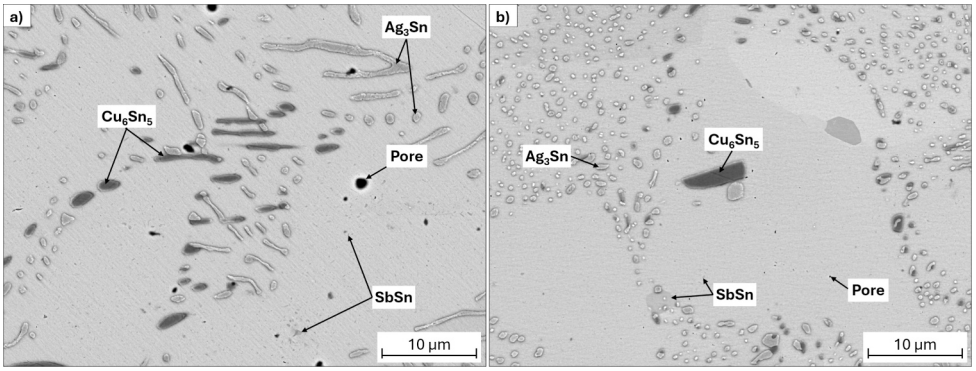

Fig. 13. BSE-SEM images a) before creep testing, b) after creep testing at 100 °C and 20 MPa.

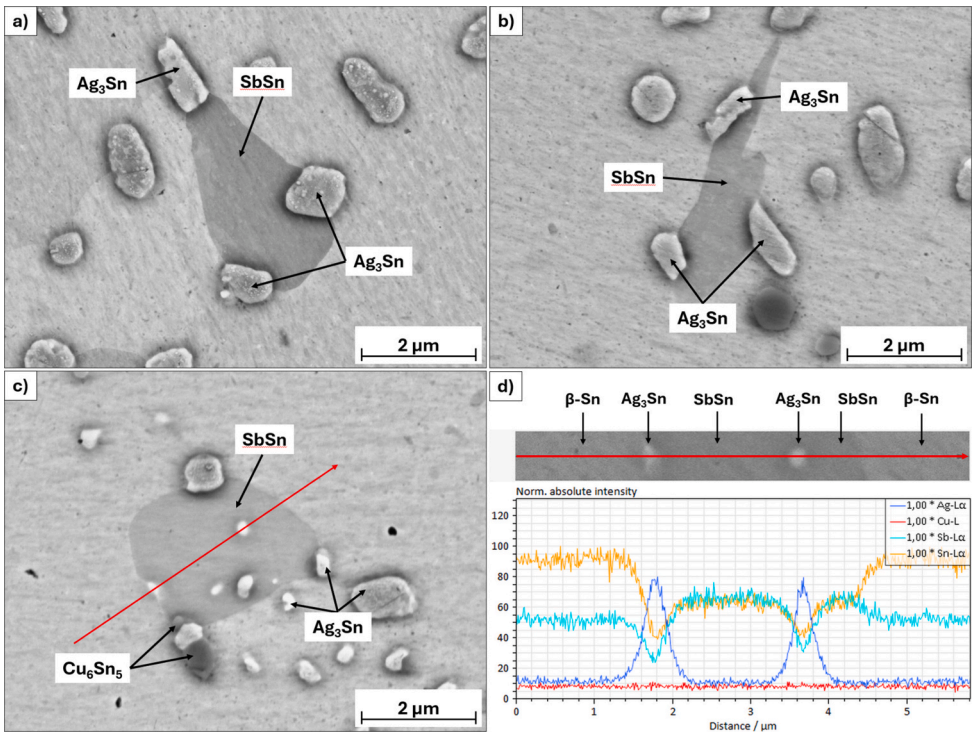

Fig. 14. BSE-SEM image of eutectic region after creep testing at a) 20 MPa and 35 °C, b) 20 MPa and 50 °C, as well as c) 20 MPa and 100 °C and d) its corresponding EDS-line-scan.

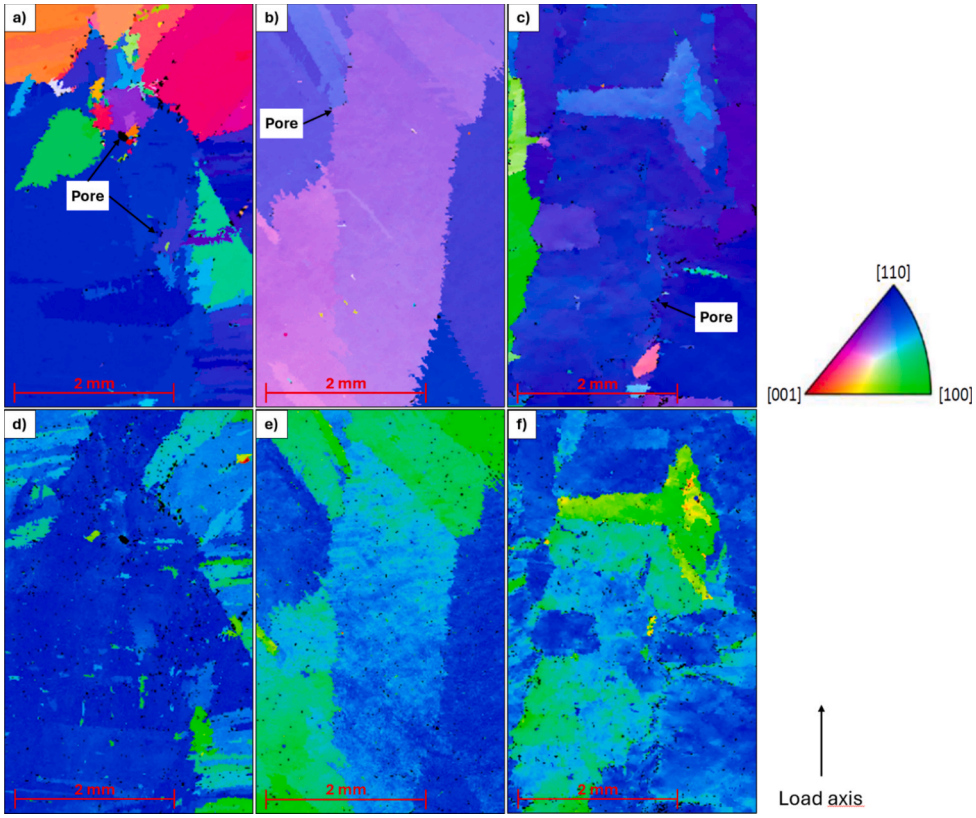

Fig. 15. EBSD maps of longitudinal cross sections after compression creep testing of samples, which were tested at an initial stress of 20 MPa and temperatures of 35 °C: a) IPFY-map, d) GAM, 50 °C: b) IPFY-map, e) GAM, or 100 °C: c) IPFY-map, f) GAM.

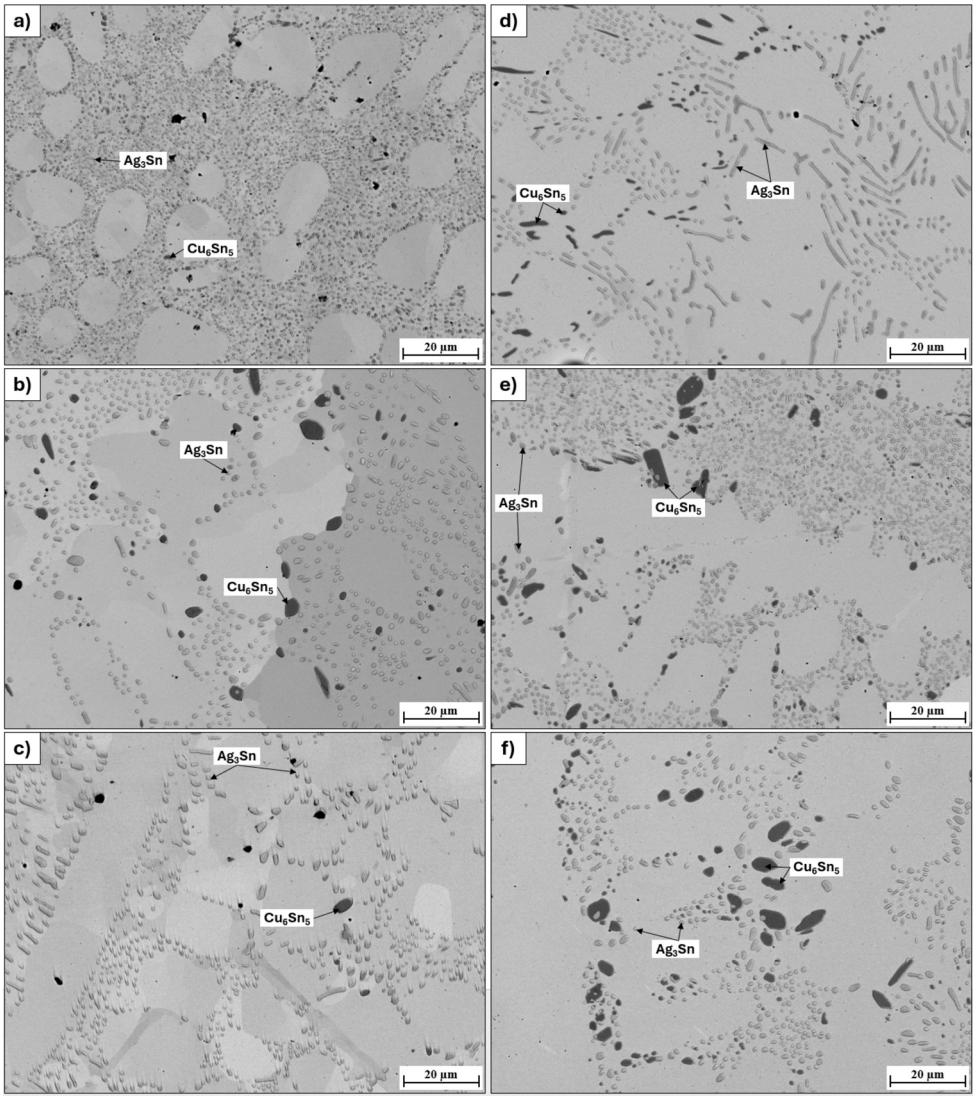

Fig. 16. BSE-SEM-images before creep testing of SAC 387, which was pre-aged at: a) 24 h at 125 °C, b) 500 h at 125 °C, c) 1500 h at 125 °C, as well as of SAC 396+, which was pre-aged at: d) 24 h at 125 °C, e) 500 h at 125 °C, f) 1500 h at 125 °C.

4. Conclusion

Compression creep testing and microstructure investigations (CALPHAD, EDS, EBSD, XRD, and TEM) of for 24 h, 500 h and 1500 h at 125 °C pre-aged samples were used to evaluate the microstructure evolution and creep behavior of alloy Sn-3.9Ag-0.6Cu-3.0Sb (SAC 396+) in comparison to alloy Sn-3.8Ag-0.7Cu (SAC 387). It was found that Sb hardened SAC 396+ showed a better creep performance at all tested creep temperatures and after isothermal ageing.

- Besides intermetallic particles of Ag_3Sn and Cu_6Sn_5, SbSn-particles were found in SAC 396+ in the β-Sn-dendrites. Beyond that, Sb is dissolved in β-Sn.
- In XRD measurements, SbSn was detected as $Sb_{0.49}Sn_{0.51}$, which exhibits a rhombohedral R-3 m crystal structure and is in coherence with literature.
- Compression creep tests of SAC 396+ were performed at temperatures of 35 °C, 50 °C, 85 °C, 100 °C and 125 °C, as well as with stresses between 7.5 MPa and 32.5 MPa. The stress exponents were in the range of 7.4–7.5 at temperatures of 100 °C or below. The stress exponent at 125 °C was 4.8, which indicates a mechanism change between 100 °C and 125 °C. This drop in stress exponent was associated with a mechanism change from dislocation climb, controlled by dislocation pipe diffusion at temperatures of 100 °C and below towards dislocation climb, controlled by lattice diffusion at 125 °C.
- Further isothermal ageing for 500 h or 1500 h at 125 °C showed a slight shift towards smaller stresses in the Norton-Plots at 50 °C, but the stress exponents were relatively stable in the range between 7.4–8.0, whereas for SAC 387, the stress exponent showed a significant increase from 8.4 to 21.4.
- The activation energies of SAC 396+ were each calculated of equivalent initial stresses at three different temperatures and are 84.7 kJ/mol at 20 MPa, 93.0 kJ/mol at 15 MPa and 99.6 kJ/mol at 12.5 MPa, indicating a dislocation creep mechanism.

Future work should focus on Sn–Ag–Cu alloys with lower Ag contents of 1.0 wt-% with Sb addition that maintain or improve the creep resistance, while the material costs in the Surface-Mount Device (SMD) assembly process is reduced due to a lower Ag content.

CRediT authorship contribution statement

Christian Kreiner: Writing – original draft, Visualization,

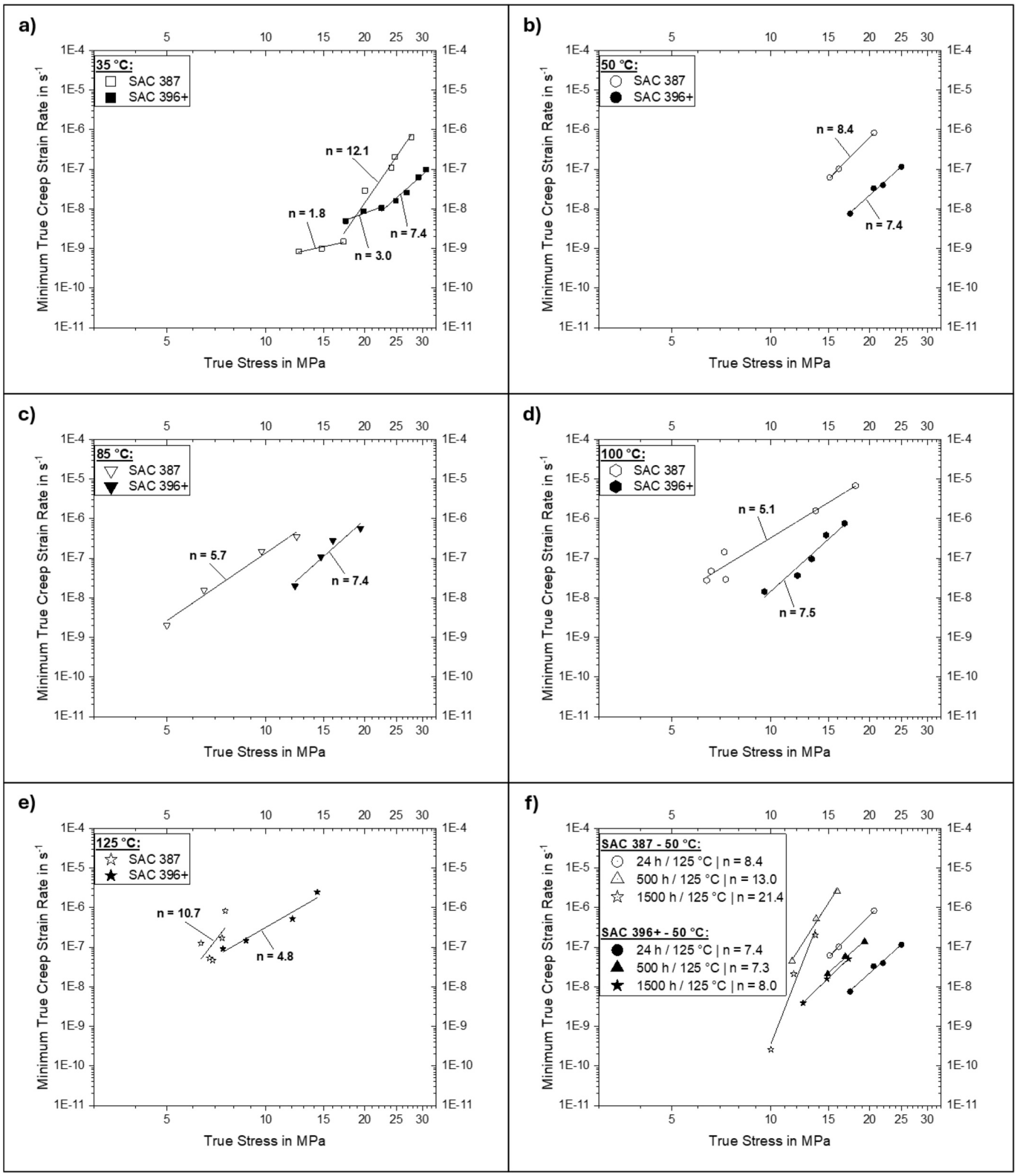

Fig. 17. Norton-Plots of SAC 396 + in comparison to SAC 387 at different compression creep test temperatures: a) 35 °C, b) 50 °C, c) 85 °C, d) 100 °C, e) 125 °C, f) comparison of 24 h at 125 °C and 500 h at 125 °C pre-aged samples after testing at 50 °C.

Validation, Project administration, Methodology, Investigation, Formal analysis, Data curation, Conceptualization. **Michael Konrad Eusterholz:** Writing – review & editing, Visualization, Validation, Resources, Methodology, Investigation, Formal analysis, Data curation. **Gabriel Benedet Dutra:** Writing – review & editing, Validation, Methodology, Data curation. **Daniel Zeitler:** Writing – review & editing, Validation, Methodology, Investigation, Formal analysis, Data curation. **Heinz Werner Höppel:** Writing – review & editing, Validation, Supervision. **Ulrich Tetzlaff:** Writing – review & editing, Validation, Supervision, Resources, Project administration, Funding acquisition,

Table 8
Measured stress exponents in the dislocation creep regime of SAC 396 + and SAC 387.

Temperature in °C	Ageing time at 125 °C					
	SAC 387			SAC 396+		
	24 h	500 h	1500 h	24 h	500 h	1500 h
35	12.1	–	–	7.4	–	–
50	8.4	13.0	21.4	7.4	7.3	8.0
85	5.7	–	–	7.4	–	–
100	5.1	–	–	7.5	–	–
125	10.7	–	–	4.8	–	–

Conceptualization.

Declaration of generative AI and AI-assisted technologies in the writing process

Statement: During the preparation of this work the authors used the AI-tool *ChatGPT-5* only for preliminary literature search for discrete topics, not involved in data analysis and conclusion writing. After using this tool/service, the authors doublechecked the suggested literature before citating. The authors take full responsibility for the content of the published article.

Funding sources

This research was funded by the Bavarian Collaborative Research Program (BayVFP) of the Free State of Bavaria under the project "MaWis-KI". The research activities were further supported by grants from the Bavarian Academic Forum (BayWISS), Joint Academic Partnership "Resource Efficiency and Materials".

Declaration of competing interest

The authors declare that they have no known competing financial interests or personal relationships that could have appeared to influence the work reported in this paper.

Acknowledgments

Special thanks are extended to the laboratory team for their support and especially to Dr. Georges Lemos for his helpful support in conducting the creep tests and the scanning electron microscopy investigations. Further thanks go to Dr. Ali Ahmadian from the Karlsruhe Institute of Technology, Germany for preparing the transmission electron microscopy images. The authors gratefully acknowledge Karlsruhe Nano Micro Facility (KNMFi) for providing advanced instruments (proposal number: 2024-032-032046).

Data availability

The data that has been used is confidential.

References

[1] S. Zhong, L. Zhang, M. Li, W. Long, F. Wang, Development of lead-free interconnection materials in electronic industry during the past decades: structure and properties, Mater. Des. 215 (2022) 110439, https://doi.org/10.1016/j.matdes.2022.110439.
[2] N.S.M. Zaimi, M.A.A.M. Salleh, M.S.A. Aziz, N.I.M. Nadzri, M.F.H. Baser, W. Tanthanuch, S. Tancharakorn, N. Mothong, C.Y. Khor, Microstructure refinement, thermal stability and mechanical properties improvements of Sn-3.0Ag-0.5Cu-xSb, Mater Charact 227 (2025) 115324, https://doi.org/10.1016/j.matchar.2025.115324.
[3] Y. Miao, T. Dong, C. Li, J. Yang, Q. Lu, Z. Xu, X. Zhang, J. Peng, J. Yi, Effects of Sb on the properties and interfacial evolution of SAC305-2Bi-xSb/Cu solder joints, J. Mater. Res. Technol. 30 (2024) 9494–9502, https://doi.org/10.1016/j.jmrt.2024.06.023.
[4] M. Ueshima, Relationship between reliability and effect of solid solution hardening at solder joints at the high temperature, in: 2012 4th Electron. Syst.-Integr. Technol. Conf., IEEE, Amsterdam, Netherlands, 2012: pp. 1–5. https://doi.org/10.1109/ESTC.2012.6542078.
[5] S. Choi, J.G. Lee, F. Guo, T.R. Bieler, K.N. Subramanian, J.P. Lucas, Creep properties of Sn-Ag solder joints containing intermetallic particles, JOM 53 (2001) 22–26, https://doi.org/10.1007/s11837-001-0098-4.
[6] T. Gu, Y. Xu, C.M. Gourlay, F.P.E. Dunne, T.B. Britton, Understanding the deformation creep and role of intermetallic compound-microstructure in Sn-Ag-Cu solders, Mater. Sci. Eng. A 918 (2024) 147429, https://doi.org/10.1016/j.msea.2024.147429.
[7] I. Dutta, C. Park, S. Choi, Impression creep characterization of rapidly cooled Sn–3.5Ag solders, Mater. Sci. Eng. A 379 (2004) 401–410, https://doi.org/10.1016/j.msea.2004.03.023.
[8] M. Kerr, N. Chawla, Creep deformation behavior of Sn–3.5Ag solder/Cu couple at small length scales, Acta Mater. 52 (2004) 4527–4535, https://doi.org/10.1016/j.actamat.2004.06.010.
[9] K.N. Subramanian, T.R. Bieler, J.P. Lucas, Microstructural engineering of solders, J. Electron. Mater. 28 (1999) 1176–1183, https://doi.org/10.1007/s11664-999-0154-3.
[10] Y. Zhang, Z. Cai, J.C. Suhling, P. Lall, M.J. Bozack, The effects of SAC alloy composition on aging resistance and reliability, in: 2009 59th Electron. Compon. Technol. Conf., IEEE, San Diego, CA, USA, 2009: pp. 370–389. https://doi.org/10.1109/ECTC.2009.5074043.
[11] Z.J. Yang, S.M. Yang, H.S. Yu, S.J. Kang, J.H. Song, K.J. Kim, IMC and creep behavior in lead-free solder joints of Sn-Ag and Sn-Ag-Cu alloy system by SP method, Int. J. Automot. Technol. 15 (2014) 1137–1142, https://doi.org/10.1007/s12239-014-0118-3.
[12] J. Thambi, A. Schiessl, M. Waltz, K.-D. Lang, U. Tetzlaff, Modified constitutive creep laws with micromechanical modeling of Pb-free solder alloys, J. Electron. Packag. 139 (2017) 031002, https://doi.org/10.1115/1.4035850.
[13] H.I. Lebda, D.M. Habashy, M.M. Mousa, Simulation and prediction of creep rate, activation energy, and rupture time of Sn94Sb5Ag1 lead-free solder alloy using artificial neural network modeling, J. Electron. Mater. 53 (2024) 5486–5504, https://doi.org/10.1007/s11664-024-11235-1.
[14] Y. Gao, X. Bian, X. Qiu, Y. Jia, J. Yi, G. Wang, Investigation of microstructure and mechanical properties of SAC105 solders with Sb, In, Ni, and Bi additions, Materials 16 (2023) 4059, https://doi.org/10.3390/ma16114059.
[15] C. Li, Y. Yan, T. Gao, G. Xu, The microstructure, thermal, and mechanical properties of Sn-3.0Ag-0.5Cu-xSb high-temperature lead-free solder, Materials 13 (2020) 4443, https://doi.org/10.3390/ma13194443.
[16] V. Shukla, O. Ahmed, G. Jalilvand, A. Mehta, P. Su, T. Jiang, Effects of aging on microstructure and mechanical properties of Sn-Ag-Cu-Bi solder alloys, in: 2021 IEEE 71st Electron. Compon. Technol. Conf. ECTC, IEEE, San Diego, CA, USA, 2021: pp. 667–672. https://doi.org/10.1109/ECTC32696.2021.00116.
[17] C.Y. Tan, M.A.A. Mohd Salleh, N. Saud, T. Nishimura, K. Nogita, Effects of vanadium on the properties of Sn-3wt%Ag-5wt%Cu solder alloy, J. Mater. Sci. Mater. Electron. 35 (2024) 1408, https://doi.org/10.1007/s10854-024-13164-5.
[18] J. Yan, B. Wang, J. Zhao, L. Zhao, R. Guo, J. Sheng, Improvement of heat aging resistance and tensile strength of SAC305/Cu solder joints by multi-element microalloying, Intermetallics 173 (2024) 108428, https://doi.org/10.1016/j.intermet.2024.108428.
[19] B. Ali, M.F.M. Sabri, I. Jauhari, N.L. Sukiman, Impact toughness, hardness and shear strength of Fe and Bi added Sn-1Ag-0.5Cu lead-free solders, Microelectron. Reliab. 63 (2016) 224–230, https://doi.org/10.1016/j.microrel.2016.05.004.
[20] U. Ali, H. Khan, M. Aamir, K. Giasin, N. Habib, M. Owais Awan, Analysis of microstructure and mechanical properties of bismuth-doped SAC305 lead-free solder alloy at high temperature, Metals 11 (2021) 1077, https://doi.org/10.3390/met11071077.
[21] H. Zhang, Z. Xu, Y. Wang, C. Tian, C. Fan, S. Motozuka, J. Yu, The effect of Bi addition on the electromigration properties of Sn-3.0Ag-0.5Cu lead-free solder, Metals 14 (2024) 1149, https://doi.org/10.3390/met14101149.
[22] X.F. Tan, Q. Hao, Q. Gu, S.D. McDonald, K. Sweatman, M. Bermingham, K. Nogita, The effects of Sb on the lattice and microstructure characteristics of hypo-eutectic Sn-Bi alloys, Mater Charact 201 (2023) 112934, https://doi.org/10.1016/j.matchar.2023.112934.
[23] R.J. McCabe, M.E. Fine, Creep of tin, Sb-solution-strengthened tin, and SbSn-precipitate-strengthened tin, Metall. Mater. Trans. A 33 (2002) 1531–1539, https://doi.org/10.1007/s11661-002-0075-8.
[24] R.J. McCabe, M.E. Fine, Unexpected transient creep behavior of tin alloys strengthened by high volume fractions of SbSn, Metall. Mater. Trans. A 33 (2002) 575–580, https://doi.org/10.1007/s11661-002-0119-0.
[25] R.J. Mccabe, M.E. Fine, High creep resistance tin-based alloys for soldering applications, J. Electron. Mater. 31 (2002) 1276–1282, https://doi.org/10.1007/s11664-002-0021-y.
[26] B. Wang, J. Yan, J. Liu, J. Zhao, L. Zhao, Ni and Sb improve the microstructure, mechanical properties, and solder joint reliability of Sn-3.0Ag-0.5Cu alloy, Vacuum 231 (2025) 113782, https://doi.org/10.1016/j.vacuum.2024.113782.
[27] P. Sungkhaphaitoon, T. Plookphol, The effects of antimony addition on the microstructural, mechanical, and thermal properties of Sn-3.0Ag-0.5Cu solder alloy, Metall. Mater. Trans. A 49 (2018) 652–660, https://doi.org/10.1007/s11661-017-4439-5.
[28] S.A. Belyakov, R.J. Coyle, B. Arfaei, J.W. Xian, C.M. Gourlay, Microstructure and damage evolution during thermal cycling of Sn-Ag-Cu solders containing antimony, J. Electron. Mater. 50 (2021) 825–841, https://doi.org/10.1007/s11664-020-08507-x.

[29] P.T. Vianco, J.A. Rejent, A.C. Kilgo, Creep behavior of the ternary 95.5Sn-3.9Ag-0.6Cu solder: part II—aged condition, J. Electron. Mater. 33 (2004) 1473–1484, https://doi.org/10.1007/s11664-004-0089-7.
[30] X. Jing, W. Sun, L. Cao, P. He, S. Zhang, Phase transformation, microstructural evolution and mechanical degradation of SnAg2.4/Cu solder joints at 160 °C high-temperature storage test, Mater Charact 221 (2025) 114802, https://doi.org/10.1016/j.matchar.2025.114802.
[31] B. Ernst, S. Keim, U. Tetzlaff, On the anisotropic indentation modulus and anisotropic creep behavior of β -Sn characterized by nanoindentation methods, Mater. Sci. Eng. A 848 (2022) 143392, https://doi.org/10.1016/j.msea.2022.143392.
[32] M. Klinger, A. Jäger, *Crystallographic Tool Box* (*CrysTBox*): automated tools for transmission electron microscopists and crystallographers, J. Appl. Crystallogr. 48 (2015) 2012–2018, https://doi.org/10.1107/S1600576715017252.
[33] A. Kanjilal, V. Jangid, P. Kumar, Critical evaluation of creep behavior of Sn-Ag-Cu solder alloys over wide range of temperatures, Mater. Sci. Eng. A 703 (2017) 144–153, https://doi.org/10.1016/j.msea.2017.07.061.
[34] G. Zeng, M.D. Callaghan, S.D. McDonald, H. Yasuda, K. Nogita, In situ studies revealing dendrite and eutectic growth during the solidification of Sn-0.7Cu-0.5Ag Pb-free solder alloy, J. Alloys Compd. 797 (2019) 804–810, https://doi.org/10.1016/j.jallcom.2019.04.153.
[35] B. Wang, X.J. Hu, W. Sun, J.L. Liao, H.L. Peng, N. Hou, B. Chen, G. Zeng, Hypo-eutectic microstructure formation and nanomechanical response in Sn-3.0Ag-0.5Cu solder balls: effects of undercooling, Mater Charact 198 (2023) 112707, https://doi.org/10.1016/j.matchar.2023.112707.
[36] L. Snugovsky, C. Cermignani, D.D. Perovic, J.W. Rutter, The solid solubility of Ag and Cu in the Sn phase of eutectic and near-eutectic Sn-Ag-Cu solder alloys, J. Electron. Mater. 33 (2004) 1313–1315, https://doi.org/10.1007/s11664-004-0159-x.
[37] L. Norén, R.L. Withers, S. Schmid, F.J. Brink, V. Ting, Old friends in a new light: "SnSb" revisited, J. Solid State Chem. 179 (2006) 404–412, https://doi.org/10.1016/j.jssc.2005.10.031.
[38] S. Chantaramanee, P. Sungkhaphaitoon, Combined effects of Bi and Sb elements on microstructure, thermal and mechanical properties of Sn-0.7Ag-0.5Cu solder alloys, Trans. Nonferrous Met. Soc. China 32 (2022) 3301–3311, https://doi.org/10.1016/S1003-6326(22)66021-7.
[39] J. Meija, T.B. Coplen, M. Berglund, W.A. Brand, P. De Bièvre, M. Gröning, N.E. Holden, J. Irrgeher, R.D. Loss, T. Walczyk, T. Prohaska, Atomic weights of the elements 2013 (IUPAC Technical Report), Pure Appl. Chem. 88 (2016) 265–291. https://doi.org/10.1515/pac-2015-0305.
[40] W. Tillmann, L. Hagen, M. Abdulgader, M.D. Kensy, M. Paulus, Microstructural characteristics in babbitt coatings deposited by LPCS, Coatings 10 (2020) 689, https://doi.org/10.3390/coatings10070689.
[41] S. Lidin, S. Piao, The structure of Cu_6 Sn_5 -Sb_x – large effects of subtle doping, Z. Für Anorg. Allg. Chem. 635 (2009) 611–613, https://doi.org/10.1002/zaac.200900018.
[42] X. Wang, H. Cui, Y. Xiong, Q. Li, X. Wang, S. Cai, Q. Wang, N. Liu, In-depth investigation of multi-element alloying on the microstructure and mechanical properties of Sn7Sb/Cu joints, J. Mater. Res. Technol. 36 (2025) 7318–7329, https://doi.org/10.1016/j.jmrt.2025.05.012.
[43] J. Donovan, J. Fellowes, B. McMorran, Average atomic number and electron backscattering in compounds, Microsc. Microanal. 25 (2019) 2314–2315, https://doi.org/10.1017/S1431927619012303.
[44] M. Čalkovský, E. Müller, D. Gerthsen, Quantitative analysis of backscattered-electron contrast in scanning electron microscopy, J. Microsc. 289 (2023) 32–47, https://doi.org/10.1111/jmi.13148.
[45] T. Kowoll, E. Müller, S. Fritsch-Decker, S. Hettler, H. Störmer, C. Weiss, D. Gerthsen, Contrast of backscattered electron SEM images of nanoparticles on substrates with complex structure, Scanning 2017 (2017) 1–12, https://doi.org/10.1155/2017/4907457.
[46] M. Wołcyrz, R. Kubiak, S. Maciejewski, X-ray investigation of thermal expansion and atomic thermal vibrations of tin, indium, and their alloys, Phys. Status Solidi B 107 (1981) 245–253, https://doi.org/10.1002/pssb.2221070125.
[47] J.A. Lee, G.V. Raynor, The lattice spacings of binary tin-rich alloys, Proc. Phys. Soc. Sect. B 67 (1954) 737–747, https://doi.org/10.1088/0370-1301/67/10/301.
[48] C. Schmetterer, J. Polt, H. Flandorfer, The phase equilibria in the Sb-Sn system – part II: experimental results, J. Alloys Compd. 743 (2018) 523–536, https://doi.org/10.1016/j.jallcom.2017.11.367.
[49] T.G. Langdon, Deformation at high temperatures, in: Strength Met. Alloys ICSMA 6, Elsevier, 1982: pp. 1105–1120. https://doi.org/10.1016/B978-1-4832-8423-1.50168-1.
[50] R. Horiuchi, M. Otsuka, Mechanism of high temperature creep of aluminum-magnesium solid solution alloys, Trans. Jpn. Inst. Met. 13 (1972) 284–293, https://doi.org/10.2320/matertrans1960.13.284.
[51] N. Matsuno, H. Oikawa, Structure change during primary creep of Al-5.5 at % Mg alloy, Scr. Metall. 15 (1981) 319–322, https://doi.org/10.1016/0036-9748(81)90352-5.
[52] A. Orlová, J. Čadek, The effect of stress changes during creep on the dislocation structure of Al-5.5 at.% Mg, Mater. Sci. Eng. 38 (1979) 139–144, https://doi.org/10.1016/0025-5416(79)90089-2.
[53] P. Yavari, T.G. Langdon, An examination of the breakdown in creep by viscous glide in solid solution alloys at high stress levels, Acta Metall. 30 (1982) 2181–2196, https://doi.org/10.1016/0001-6160(82)90139-0.
[54] M. Moriuchi, Y. Kariya, M. Kondo, Y. Kanda, Class I creep deformation of Sn–Ag–Cu containing solid solution elements and its effect on thermal fatigue life of solder joints, Mater. Trans. 63 (2022) 805–812, https://doi.org/10.2320/matertrans.MT-MC2022015.
[55] M.D. Mathew, H. Yang, S. Movva, K.L. Murty, Creep deformation characteristics of tin and tin-based electronic solder alloys, Metall. Mater. Trans. A 36 (2005) 99–105, https://doi.org/10.1007/s11661-005-0142-z.
[56] T. Chen, I. Dutta, Effect of Ag and Cu concentrations on the creep behavior of Sn-based solders, J. Electron. Mater. 37 (2008) 347–354, https://doi.org/10.1007/s11664-007-0340-0.
[57] P.T. Vianco, J.A. Rejent, A.C. Kilgo, Creep behavior of the ternary 95.5Sn-3.9Ag-0.6Cu solder—part I: as-cast condition, J. Electron. Mater. 33 (2004) 1389–1400, https://doi.org/10.1007/s11664-004-0169-8.
[58] A.A. El-Daly, A.E. Hammad, A. Fawzy, D.A. Nasrallh, Microstructure, mechanical properties, and deformation behavior of Sn–1.0Ag–0.5Cu solder after Ni and Sb additions, Mater. Des. 43 (2013) 40–49, https://doi.org/10.1016/j.matdes.2012.06.058.
[59] J.H.L. Pang, B.S. Xiong, Mechanical properties for 95.5Sn-3.8Ag-0.7Cu lead-free solder alloy, IEEE Trans. Compon. Packag. Technol. 28 (2005) 830–840. https://doi.org/10.1109/TCAPT.2005.848587.
[60] Qian Zhang, A. Dasgupta, P. Haswell, Viscoplastic constitutive properties and energy-partitioning model of lead-free Sn3.9Ag0.6Cu solder alloy, in: 53rd Electron. Compon. Technol. Conf. 2003 Proc., IEEE, New Orleans, Louisiana, USA, 2003: pp. 1862–1868. https://doi.org/10.1109/ECTC.2003.1216558.
[61] H.G. Song, J.W. Morris, F. Hua, The creep properties of lead-free solder joints, JOM 54 (2002) 30–32, https://doi.org/10.1007/BF02701846.
[62] W.J. Plumbridge, C.R. Gagg, S. Peters, The creep of lead-free solders at elevated temperatures, J. Electron. Mater. 30 (2001) 1178–1183, https://doi.org/10.1007/s11664-001-0147-3.
[63] J.E. Breen, J. Weertman, Creep of polycrystalline tin, JOM 7 (1955) 1230–1234, https://doi.org/10.1007/BF03379034.
[64] D.R. Shirley, J.K. Spelt, Primary creep in Sn-3.8Ag-0.7Cu solder, part II: constitutive creep model development and finite element analysis, J. Electron. Mater. 38 (2009) 2388–2397, https://doi.org/10.1007/s11664-009-0906-0.
[65] P.O. Guglielmi, M. Ziehmer, E.T. Lilleodden, On a novel strain indicator based on uncorrelated misorientation angles for correlating dislocation density to local strength, Acta Mater. 150 (2018) 195–205, https://doi.org/10.1016/j.actamat.2018.03.009.
[66] X.J. Hu, W. Sun, J.L. Liao, Y.H. Zhang, B. Wang, S.S. Shuai, C. Liu, G. Zeng, The influences of microstructural length scale on the tensile properties and deformation mechanisms of Sn-3.0Ag-0.5Cu solder alloys, Mater. Sci. Eng. A 916 (2024) 147300, https://doi.org/10.1016/j.msea.2024.147300.
[67] J. Gong, C. Liu, P.P. Conway, V.V. Silberschmidt, Modelling of Ag3Sn coarsening and its effect on creep of Sn–Ag eutectics, Mater. Sci. Eng. A 427 (2006) 60–68, https://doi.org/10.1016/j.msea.2006.04.034.
[68] J. Keller, D. Baither, U. Wilke, G. Schmitz, Mechanical properties of Pb-free SnAg solder joints, Acta Mater. 59 (2011) 2731–2741, https://doi.org/10.1016/j.actamat.2011.01.012.
[69] L. Liu, Y. Yao, T. Zeng, L.M. Keer, A micromechanical model considering dislocation density based intra-granular backstress under cyclic loading, Mech. Mater. 129 (2019) 41–49, https://doi.org/10.1016/j.mechmat.2018.10.011.